CONTROL OF SEPARATION USING PULSED WALL JETS:

NUMERICAL INVESTIGATIONS USING DNS AND LES

AFOSR Grant Number F49620-97-1-0274

Final Report

by

Hermann F. Fasel

Department of Aerospace and Mechanical Engineering

The University of Arizona

Tucson, AZ 85721

Submitted to

The Air Force Office of Scientific Research

March 2000

AFRL-SR-BL-TR-01-

0099

REPORT DOCUMENTATION PAGE

Public reporting burden for this collection of information is estimated to average 1 hour per response, including th... gathering and maintaining the data needed, and completing and reviewing the collection of information. Send com... collection of information, including suggestions for reducing this burden, to Washington Headquarters Services, Dir... Davis Highway, Suite 1204, Arlington, VA 22202-4302, and to the Office of Management and Budget, Paperwork Reduction Project (0704-0188), Washington, DC 20503.

1. AGENCY USE ONLY (Leave blank)	2. REPORT DATE	3. REPORT TYPE AND DATES COVERED
	12/13/00	Final Technical(01/01/98-12/31/99)

4. TITLE AND SUBTITLE
Control of Separation Using Pulsed Wall Jets:
Numerical Investigations Using DNS and LES

5. FUNDING NUMBERS
F49620-97-1-0274

6. AUTHOR(S)
Hermann F. Fasel

7. PERFORMING ORGANIZATION NAME(S) AND ADDRESS(ES)
Aerospace and Mechanical Engineering
The College of Engineering and Mines
The University of Arizona
Tucson, AZ 85721

8. PERFORMING ORGANIZATION REPORT NUMBER

9. SPONSORING/MONITORING AGENCY NAME(S) AND ADDRESS(ES)
AFOSR/NA
801 N. Randolph St
Arlington, VA 22202-1977

10. SPONSORING/MONITORING AGENCY REPORT NUMBER

11. SUPPLEMENTARY NOTES

12a. DISTRIBUTION/AVAILABILITY STATEMENT

Approved for Public Release
Distribution is Unlimited

AIR FORCE OFFICE OF SCIENTIFIC RESEARCH (AFOSR)
NOTICE OF TRANSMITTAL DTIC. THIS TECHNICAL REPORT
HAS BEEN REVIEWED AND IS APPROVED FOR PUBLIC RELEASE
LAW AFR 190-12. DISTRIBUTION IS UNLIMITED.

13. ABSTRACT (Maximum 200 words)

In a numerical effort, the dynamics of coherent structures in unforced, and periodically forced, turbulent weak wall jets has been investigated. The objective of this research is to better understand the effect of pulsed blowing used for separation control on airfoils. The focus has been on flat plate geometries. In the simulations, weak wall jets are generated by steady and/or pulsed wall-tangential blowing through a wall-slot into a constant pressure or adverse pressure-gradient boundary layer. Numerical approaches taken are Direct Numerical Simulations (DNS), Large-Eddy Simulations (LES), and Unsteady Reynolds-Averaged Navier-Stokes calculations (URANS). Using three-dimensional LES, it was shown that large-amplitude pulsed blowing can prevent flow separation. However, in order to draw definite quantitative conclusions regarding the evolution of two-dimensional coherent structures generated by pulsed blowing, additional simulations with better grid resolution would be required. Such simulations are computationally very expensive. Therefore, at much lower computational expense, two-dimensional URANS was employed for parameter studies of the nonlinear instability of the weak wall jet. High frequency forcing was found to produce disturbances that grow initially, while disturbances are always damped for low frequency forcing. For large forcing amplitudes, however, low frequency disturbances, while damped, appear to persist over a longer streamwise distance.

14. SUBJECT TERMS	15. NUMBER OF PAGES
	57
	16. PRICE CODE

17. SECURITY CLASSIFICATION OF REPORT	18. SECURITY CLASSIFICATION OF THIS PAGE	19. SECURITY CLASSIFICATION OF ABSTRACT	20. LIMITATION OF ABSTRACT
UNCLASSIFIED	UNCLASSIFIED	UNCLASSIFIED	UNLIMITED

CONTROL OF SEPARATION USING PULSED WALL JETS: NUMERICAL INVESTIGATIONS USING DNS AND LES

AFOSR GRANT F49620-97-1-0274

Hermann F. Fasel

Department of Aerospace and Mechanical Engineering

The University of Arizona, Tucson

Abstract

In a numerical/theoretical effort, the dynamics of coherent structures in unforced, and periodically forced, turbulent *weak* wall jets has been investigated. The objective of this research is to better understand the effect of pulsed blowing used for separation control on airfoils. The focus has been on flat plate geometries. In the simulations, a weak wall jet is generated by steady and/or pulsed wall-tangential blowing through a wall-slot into a constant pressure or adverse pressure gradient boundary layer. Numerical approaches taken are Direct Numerical Simulations (DNS), Large-Eddy Simulations (LES), and Unsteady Reynolds-Averaged Navier-Stokes calculations (URANS). Using three-dimensional LES, it was shown that large-amplitude pulsed blowing can prevent flow separation. However, in order to draw definite quantitative conclusions regarding the evolution of two-dimensional coherent structures generated by pulsed blowing, additional simulations with better grid resolution would be required. Such simulations are computationally very expensive. Therefore, at much lower computational expense, two-dimensional URANS was employed for parameter studies of the nonlinear instability of the weak wall jet. It was found that forcing at high frequencies produces disturbances that grow initially, while disturbances are always damped for low frequency forcing. For large forcing amplitudes, however, it appears that low frequency disturbances, while damped, persist over a longer streamwise distance.

1 Motivation / Background

Experimental research by Wygnanski and co-workers (Wygnanski 1997) has provided considerable evidence that periodically forced wall jets (tangential oscillatory blowing) may be an effective method for the control of separation of flows over single-element or segmented airfoils (including flaps). However, many of the fundamental mechanisms that are responsible for the often striking effect of oscillatory blowing were not understood. Therefore, in close collaboration with the experimental effort, direct numerical simulations (DNS), large-eddy simulations (LES), and stability investigations have being carried out for typical wall jet configurations. These configurations arise when periodic forcing is applied for separation control in practical applications, e.g., separation control for flows over airfoil/flaps. To this end, we have performed numerical simulations for weak wall jets, that is, for wall jets that are embedded in a strong external stream. Future simulations are also planned for wall jets over curved surfaces. The work described is a continuation of a research effort funded previously by AFOSR, where the major emphasis has been on strong wall jets (no external stream or a weak external stream) and for flat plate surfaces only. Most of the necessary numerical tools required for the present (and future) numerical simulations were developed during this previous research effort (e.g. Navier-Stokes codes for DNS and LES).

The goal of the present research effort has been, with the joint experimental/numerical approach, to uncover the governing physical mechanisms responsible for the striking effect of oscillatory blowing on separation, and thus provide the physical understanding required to further develop this technique for practical use. Towards this end we have performed simulations using simplified model geometries that allow a reliable investigation of the relevant mechanisms and prevent contamination by effects that are not relevant.

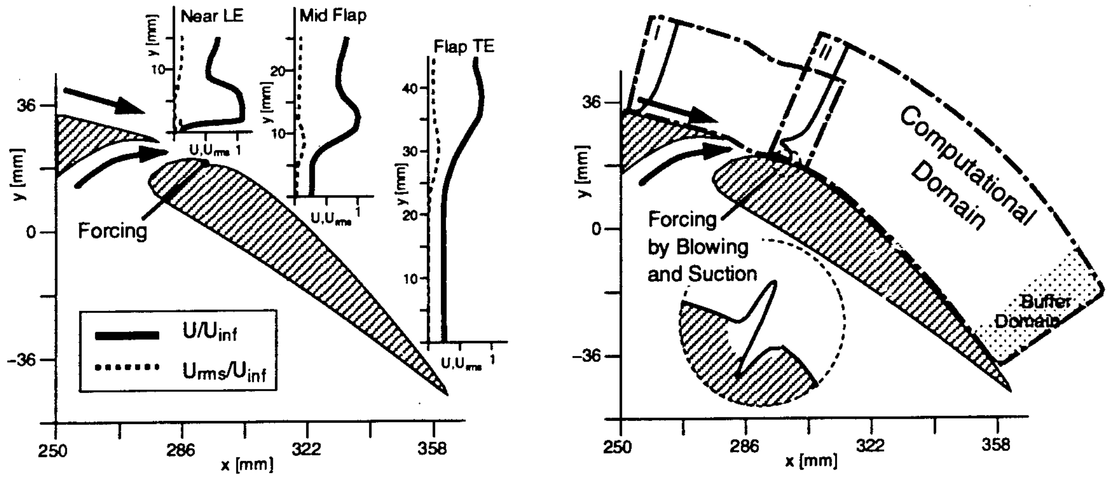

a) Experiment by Seifert et al. (1994)

b) Numerical Simulation (DNS/LES)

Figure 1: Flow over a slotted flap with oscillatory forcing.

Over the past decade, a great amount of experimental work has been performed by Wygnanski and coworkers (Wygnanski 1997) which clearly demonstrates the effectiveness of using pulsed wall jets for delaying separation. The setup of one such experiment (Seifert et al. 1994) is illustrated in Figure 1a. In the experiment, a high momentum jet that is blown through the slot along the upper surface of the flap is periodically forced at the location indicated in Figure 1a. The additional forcing strongly improves the effectiveness of the weak wall jet in preventing separation, and thus allows for significantly higher angles of attack. The effectiveness of using pulsed wall jets for delaying separation has been clearly demonstrated in experiments (Seifert et al.1993, 1996, Wygnanski 1997).

While use of LES and DNS for flows over actual slotted flaps are the final goal of our computational research (Figure 1b), several intermediate steps must be taken first to explore different aspects of this complex flow geometry. Clearly, for wall jets over actual slotted flaps, the combined effects of adverse pressure gradient and curvature plays a major role. To isolate the relevant mechanisms, this complex flow geometry

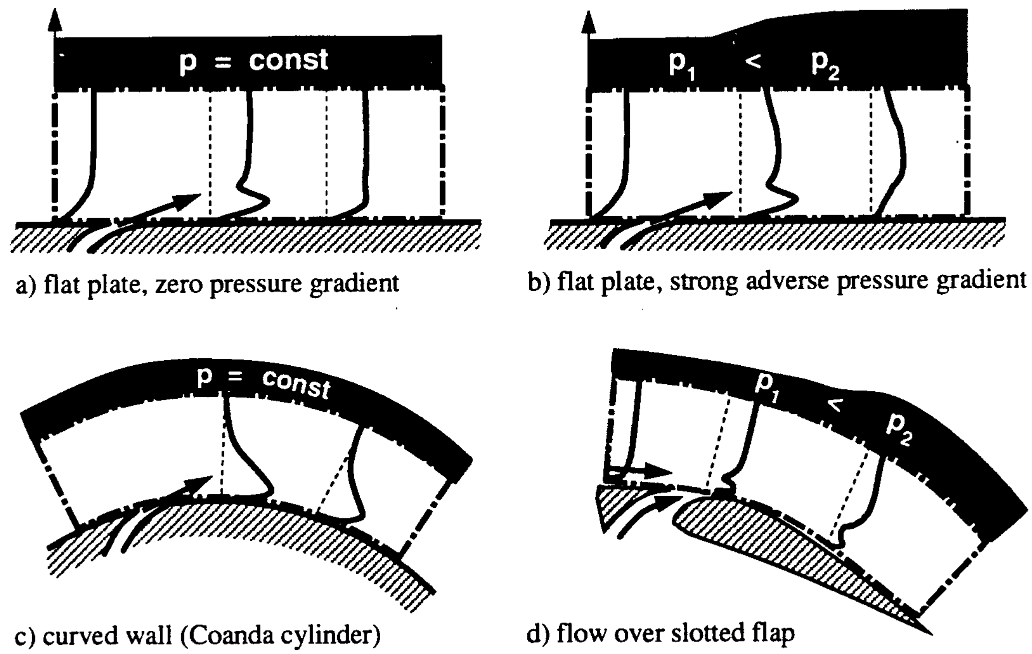

Figure 2: Generic wall jet configurations for investigating different aspects of the flow over a slotted flap.

is first broken down into simpler modules so that the effect of pressure gradient and curvature can be investigated separately.

These intermediate steps are outlined in Figure 2. During the first year of the present research project we have focussed on turbulent weak wall jets with zero free stream pressure gradient (Figure 2a). Typical results from these simulations will be discussed below. In the second year, we have investigated turbulent weak wall jets subjected to strong adverse pressure gradients (Figure 2b). The effect of curvature will be studied as part of the new research project (AFOSR GRANT F49620-00-1-0069), at first for a strong wall jet over a curved wall geometry (constant curvature, Coanda flow (Figure 2c). Ultimately, the entire flow over a slotted flap will be investigated where the effects of pressure gradient and curvature are present simultaneously (Figure 2d).

2 Computational Method

The Navier-Stokes codes employed for our numerical investigations were originally developed in our research group for boundary layer transition (see Meitz and Fasel, 2000) and have since been adapted to the wall jet flow geometry.

2.1 Governing Equations

In our codes, the complete incompressible Navier-Stokes equations are solved in vorticity-velocity formulation. Regardless of which form of time averaging or spatial filtering is applied, the resulting equations take on the form,

$$\frac{\partial \overline{\vec{\omega}}}{\partial t} + \nabla \times \left(\overline{\vec{\omega}} \times \overline{\vec{V}} - \nabla \cdot \vec{\vec{\tau}} \right) = \frac{1}{Re} \nabla^2 \overline{\vec{\omega}} . \tag{1}$$

The overbar on the velocity vector $\vec{V}$ and on the vorticity vector $\vec{\omega}$ denotes the operation of averaging the appropriate components of the corresponding vector. The quantity $\vec{\vec{\tau}} = [\tau_{ij}]$ is the turbulent stress tensor which must be modeled. Equation (1) is non-dimensionalized by the free-stream velocity U_∞, a reference length L, and a global Reynolds number defined as $Re = U_\infty L / \nu$ where ν is the kinematic viscosity. In addition to the transport equations for the vorticities, the governing equations also include a set of Poisson equations for the velocities. From the definition of vorticity and the fact that both the velocity and the vorticity fields are solenoidal, three equations for the velocity components are obtained (for more details see Meitz and Fasel, 2000). The transport equations for the vorticities and the Poisson equations for the velocities form a nearly complete system of governing equations. In order to obtain closure, a set of relations is needed for the turbulent stress tensor $[\tau_{ij}]$. These equations are provided in the form of our new Flow Simulation Methodology (FSM), see section 2.3.

2.2 Smagorinsky Subgrid-scale Model

For the LES of turbulent wall jets, as a first step, a basic Smagorinsky-type subgrid-scale model (suggested by Speziale 1995) was implemented into the Navier-Stokes code using a constant Smagorinsky coefficient. The model assumes that the sgs stresses follow a gradient-diffusion process, similar to molecular motion. Thus,

$$\tau_{ij} = \tau_{ij}^{LES} = -2\nu_T \overline{S}_{ij}, \tag{2}$$

where ν_T is the effective viscosity of the subgrid scales,

$$\nu_T = l^2 \sqrt{2\overline{S}_{ij}\overline{S}_{ij}}, \tag{3}$$

where

$$l = C_s \left(1 - e^{-(y^+/A^+)^3}\right) (\Delta_x \Delta_y \Delta_z)^{1/3} \tag{4}$$

and $C_s = 0.065$ is the Smagorinsky constant. Δ_x, Δ_y and Δ_z are the grid widths in the x, y and z directions, respectively.

This baseline eddy-viscosity model performs reasonably well for LES of zero-pressure gradient weak wall jets. However, from preliminary calculations we know that this baseline model cannot properly estimate the subgrid-scale stress for more complex flows (such as wall jet flows with strong adverse pressure gradients) which may be close to separation (Figure 2c). Therefore, we have implemented a new subgrid-scale model into the wall jet code.

2.3 New Flow Simulation Methodology (FSM)

In collaboration with C. Speziale (1998), we have been developing a new Flow Simulation Methodology (FSM) to be applicable for complex turbulent flows. A key feature of this new FSM is that it is consistent with DNS for fine grid resolution and with Reynolds-Averaged Navier-Stokes (RANS) calculations for coarse grid resolution.

This is achieved by modeling of the turbulent stress tensor $[\tau_{ij}]$ used in equation (1) as

$$\tau_{ij} = f(\Delta/L_k)\,\tau_{ij}^R\,, \tag{5}$$

where τ_{ij}^R is the Reynolds stress tensor, and $f(\Delta/L_k)$ is the so-called contribution function. The terms $\Delta = [(dx^2 + dy^2 + dz^2)/3]^{1/2}$ and $L_k = \nu^{3/4}/\epsilon^{1/4}$ are the representative computational grid size and the Kolmogorov length scale, respectively. In the coarse grid limit, $f(\Delta/L_k) \to 1$, a RANS calculation is recovered. In the fine grid limit, $f((\Delta/L_k) \to 0$, the FSM approaches a Direct Numerical Simulation (DNS). A detailed discussion of how to design an appropriate contribution function $f(\Delta/L_k)$ is given by Zhang et al. (2000).

For the Reynolds stress τ_{ij}^R in equation (5), the Algebraic Stress Model (ASM) of Gatski and Speziale (1993) is used that allows for a misalignment between the stress and strain rate tensor as it occurs in non-equilibrium flows.

$$\begin{aligned}\tau_{ij}^R = \frac{2}{3}K\delta_{ij} - f(\eta,\xi)\Big[\alpha_1\frac{k^2}{\epsilon}\overline{S}_{ij} + \alpha_2\frac{k^3}{\epsilon^2}\left(\overline{S}_{ik}\overline{W}_{kj} + \overline{S}_{jk}\overline{W}_{ki}\right) \\ -\alpha_3\frac{k^3}{\epsilon^2}\left(\overline{S}_{ik}\overline{S}_{kj} - \frac{1}{3}\overline{S}_{kl}\overline{S}_{kl}\delta_{ij}\right)\Big]\end{aligned} \tag{6}$$

Regularization is performed on the function $f(\eta,\xi)$ to remove the possibility of division by zero yielding,

$$f(\eta,\xi) = \frac{3}{3 - 2\eta^2 + 6\xi^2} \approx \frac{3(1+\eta^2)}{3 + \eta^2 + 6\eta^2\xi^2 + 6\xi^2}\,. \tag{7}$$

The terms η and ξ are the irrotational strain rate invariant and the rotational strain rate invariant, respectively. They depend on $\overline{S}_{ij}$ and $\overline{W}_{ij}$ in the following way:

$$\eta = \frac{1}{2}\frac{\alpha_3}{\alpha_1}\left(\overline{S}_{ij}\overline{S}_{ij}\right)^{1/2}\frac{k}{\epsilon}, \tag{8}$$

$$\xi = \frac{\alpha_2}{\alpha_1}\left(\overline{W}_{ij}\overline{W}_{ij}\right)^{1/2}\frac{k}{\epsilon}. \tag{9}$$

The values of coefficients appearing in equations (6), (8) and (9) are $\alpha_1 = 0.227$, $\alpha_2 = 0.0423$, and $\alpha_3 = 0.0396$.

The quantities k and ϵ appearing in equation (6) are the turbulent kinetic energy and the turbulent dissipation rate. They are computed from a standard set of turbulent transport equations,

$$\frac{Dk}{Dt} = -\tau_{ij}\frac{\partial \overline{u}_i}{\partial x_j} - \epsilon + \frac{\partial}{\partial x_j}\left[\left(\frac{\nu_T}{\sigma_k} + \frac{1}{Re}\right)\frac{\partial k}{\partial x_j}\right] \tag{10}$$

$$\frac{D\epsilon}{Dt} = -C_{\epsilon 1}\frac{\epsilon}{k}\tau_{ij}\frac{\partial \overline{u}_i}{\partial x_j} - C_{\epsilon 2} f_{\epsilon 2}\frac{\epsilon^2}{k} + \frac{\partial}{\partial x_j}\left[\left(\frac{\nu_T}{\sigma_\epsilon} + \frac{1}{Re}\right)\frac{\partial \epsilon}{\partial x_j}\right]. \tag{11}$$

Auxiliary relations, including an expression for the eddy-viscosity ν_T and wall damping functions are,

$$\nu_T = C_\mu f_\mu k^2/\epsilon, \quad f_\mu = 1 - e^{-y^+/A^+}, \tag{12}$$

$$f_{\epsilon 2} = 1 - e^{-y\,Re\sqrt{k}/10}. \tag{13}$$

The constants needed for the computation of equations (10) through (12) are,

$$C_\mu = 0.09, \quad C_{\epsilon 1} = 1.44, \quad C_{\epsilon 2} = 1.83,$$

$$\sigma_k = 1, \quad \sigma_\epsilon = 1.3, \quad A^+ = 25.$$

2.4 Numerical Scheme

A detailed review of the numerical schemes used for the solution of equation (1) and the Poisson equations for the velocities can be found in Meitz and Fasel (2000). In summary, the time dependent spatially varying flow field is calculated using the so-called spatial model (inflow–outflow). For the time integration a fourth-order accurate explicit Runge-Kutta scheme is employed. Spatial derivatives in the streamwise direction are approximated by fourth-order compact differences employing upwind biased and downwind biased switching. Wall-normal derivatives are computed with fourth-order compact differences that allow for grid stretching. Pseudo-spectral decomposition is utilized in the spanwise direction, z. Lastly, a fast Poisson solver is implemented for solving the Poisson equations for the velocity components.

The FSM requires simultaneous solution of the $k-\epsilon$ equations (see section 2.3). Space and time dependent values for k, ϵ are required for the contribution function $f(\Delta/L_k)$ (to determine L_k) and for modeling of τ_{ij}^R. The time dependent k and ϵ equations (see section 2.3) are solved using an ADI method with second-order accuracy both in space and in time. The spatial derivatives of the turbulent stresses are computed using the same difference approximation as for the computation of the resolved scales as discussed above.

3 Validation of the new FSM

The Navies-Stokes code used for all our computations has been extensively validated in the past (Meitz and Fasel, 2000). Also, the code used for our Large-Eddy Simulations using the Smagorinsky model has been tested for numerous flow configurations (see e.g. Fasel et al., 1997). However, the code extensions required for our URANS calculations and the new FSM needed to undergo a series of benchmark calculations. In these calculations, the code's capability to capture correctly the various aspects of the present very complex flow configuration was thoroughly tested.

3.1 Turbulent Boundary Layer

The performance of the FSM code has been evaluated extensively for turbulent boundary layers without and with adverse pressure gradient in the RANS limit and using the FSM as an LES. Results from these investigations have been published by Zhang et al. (2000a, 2000b). Both, mean flow and turbulence statistics, match experimental findings reported in the literature very well. One test case for FSM calculations in the RANS limit is now briefly discussed, since the turbulent boundary layer computed in these particular calculations also serves as the base flow for the URANS calculations in section 5. In Figure 3, profiles for several flow quantities from RANS calculations with various turbulence models are compared in wall-coordinates ($Re_\theta = 2525$). The turbulence models examined are the Baldwin-Lomax model, two standard $k-\epsilon$ models using near-wall corrections, MK and SSA [Myong and Kasagi (1990) and Sarkar and So (1997)], and the ASM model by Gatski and Speziale (1993).[1] As shown in Figure 3a, for all turbulence models considered the streamwise velocities agree well with the log-law. All models are also in close agreement for the Reynolds stress (Figure 3b), except very close to the wall ($y^+ < 20$). The discrepancy near the wall is much

[1] Calculations using the boundary layer approximation (ASM-RABL) and using the full Navier-Stokes equations (ASM-RANS).

more pronounced for the turbulent kinetic energy k and the turbulent dissipation rate ϵ shown in Figures 3b and 3c respectively. For comparison, results from a DNS by Spalart (1988) and from experimental measurements by Karlsson and Johansson (1988) are also shown in these graphs. For $y^+ < 100$, the models by Myong and Kasagi and Sarkar and So clearly agree much better with the DNS and the experiment. This has to be expected, since both models employ empirical near-wall damping functions that are tuned to match the asymptotic near-wall behavior of the DNS. The ASM, on the other hand, minimizes the use of wall-damping functions at the price of an incorrect asymptotic behavior near the wall. However, in all our calculations this deficiency had no impact on the quality of the flow field, clearly because the Reynolds stress computed using k and ϵ is very small where the turbulence models disagree significantly (see close up in Figure 3b). In summary, the ASM used in our URANS calculation performs very well for the turbulent boundary layer without the use of empirical near-wall corrections.

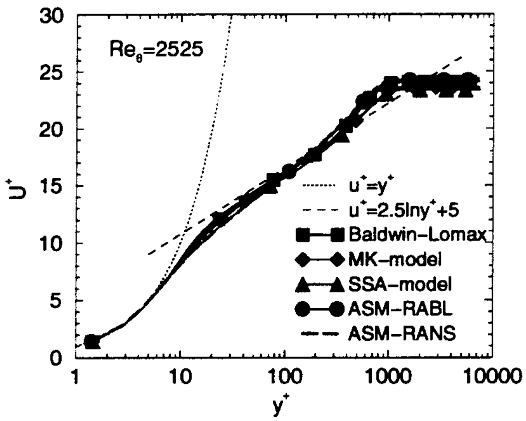

a) streamwise velocity

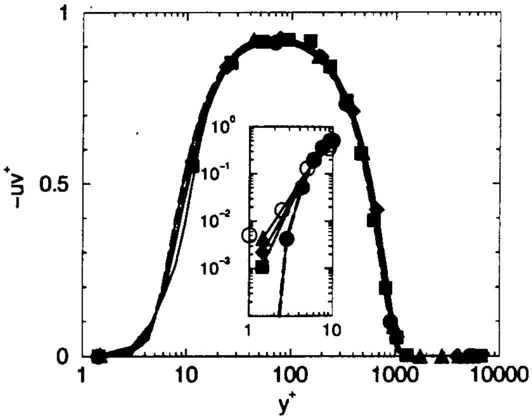

b) Reynolds stress

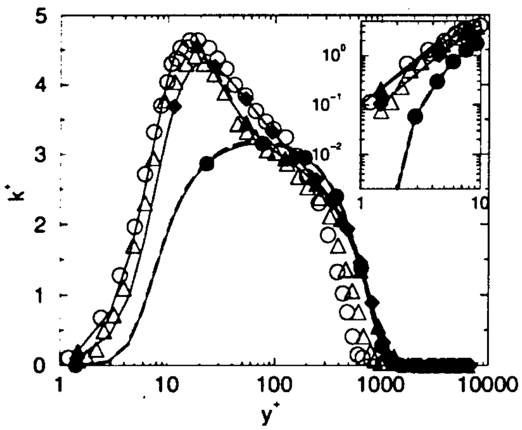

c) turbulent kinetic energy

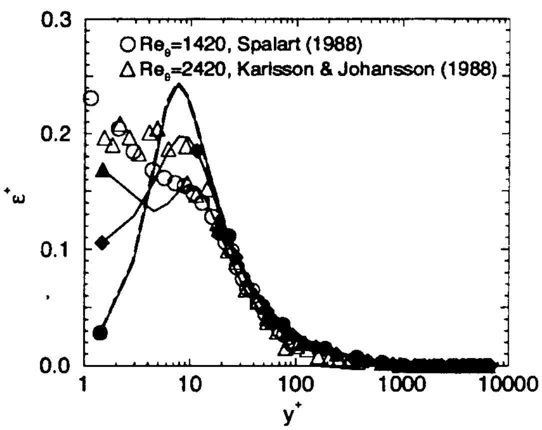

d) turbulent dissipation rate

Figure 3: Performance of the RANS-solver for the turbulent boundary layer without wall blowing. Results from several RANS calculations using different turbulence models are compared. Also shown are turbulent kinetic energy and turbulent dissipation rate from a DNS by Spalart (1988) and from experimental measurements by Karlsson and Johansson (1988).

3.2 Turbulent Strong Wall Jet

The turbulent strong wall jet represents another crucial test case, since, in addition to a boundary layer, it includes one free shear layer (as opposed to two free shear layers for the weak wall jet). Unlike for weak wall jets, there are numerous experimental and computational investigations available for comparison. As an example, a comparison with the experiments by Eriksson et al. (1998) for a jet exit $Re_j = 10000$ is shown in Figure 4 for the same $k-\epsilon$ models (MK, SSA, and ASM) and the same flow quantities as for the turbulent boundary layer discussed in the previous paragraph. Again, ASM agrees well with MK and SSA for streamwise velocity (Figure 4a) and Reynolds stress (Figure 4b), despite the asymptotically incorrect behavior for k and ϵ (Figures 4c and d). In fact, all turbulence models exhibit similar characteristics as for the turbulent boundary layer, except they all undershoot the streamwise velocity profile from the experiment which is a well-known deficiency of two-equation models.

In order to demonstrate the capability of our method to accurately capture large coherent structures in wall jet flows, we have performed a detailed comparison with experiments by Katz et al. (1992) on forced strong wall jets. The results were extremely encouraging. Not only were we able to match mean flov and eigenfunctions of the experiments extraordinarily well, but we could also provide a possible explanation for the mismatch between the dominating measured frequency in the inner and the outer region of the wall jet. Our findings are detailed in a paper presented at the Fluids 2000 conference in Denver, CO (Seidel and Fasel, 2000). A copy of the paper is attached to this report.

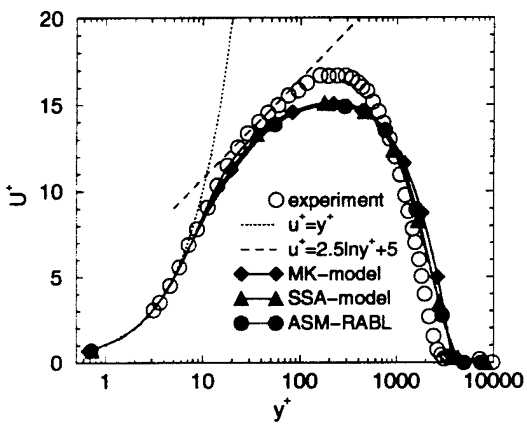

a) streamwise velocity

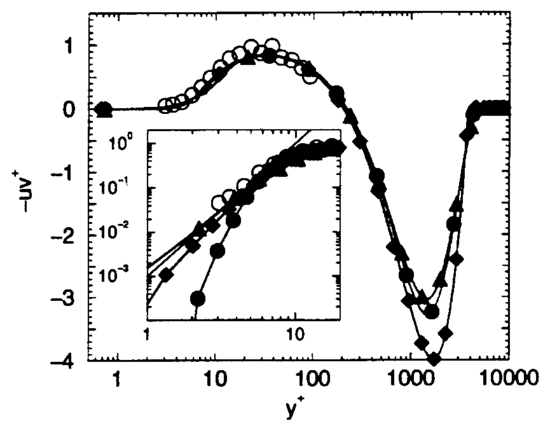

b) Reynolds stress

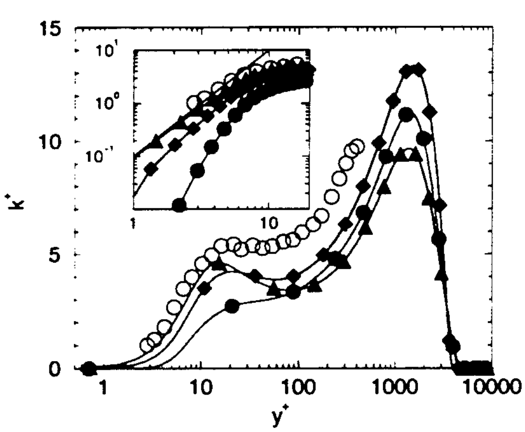

c) turbulent kinetic energy

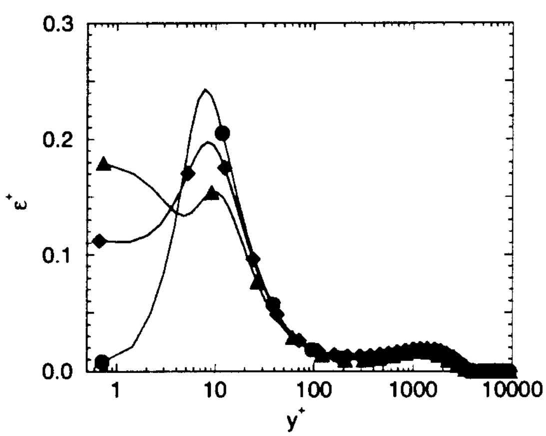

d) turbulent dissipation rate

Figure 4: Performance of the RANS-solver for the turbulent strong wall jet. Results from several RANS calculations using different turbulence models are compared. Also shown are experimental measurements by Eriksson et al. (1998).

3.3 Turbulent Weak Wall Jet

For further testing of the model we performed RANS calculations of a turbulent weak wall jet which was generated by blowing into a turbulent boundary layer through a slot at a shallow angle (geometry in Figure 2b). Over the blowing slot, streamwise and wall-normal velocity profiles are specified. This simple approach for modeling the blowing slot, while allowing for some flow adjustment close to the slot, produces the correct downstream development of the wall jet, as was demonstrated in earlier simulations (DNS of laminar wall jets, LES of turbulent wall jets using the Smagorinsky baseline model).

For the new LES, a Dirichlet boundary condition is also imposed for the turbulent kinetic energy ($k_{slot} > 0$). k_{slot} provides a measure for the turbulence level within the injected fluid. We have verified that the choice of k_{slot} only influences the flow close to the blowing slot and is not crucial for the development of the weak wall jet further downstream. This is illustrated in Figure 5, where the streamwise development of the wall jet velocity is compared for three different RANS calculations: ASM with $k_{slot} = 0.012$ (case 1), standard $k-\epsilon$ model with $k_{slot} = 0.012$ (case 2), standard $k-\epsilon$ model with $k_{slot} = 0.002$ (case 3). While the three cases differ close to the blowing slot, they are all in good agreement further downstream. Over the blowing slot, the standard $k-\epsilon$ model is certainly not well calibrated, and, as a result, it is very dissipative (case 2). Consequently, the weak wall jet initially decays more rapidly than for the ASM (case 1). This can be offset by reducing k_{slot}. The $k-\epsilon$ model (case 3) then matches the ASM result (case 1) even close to the slot.

An important feature of the new FSM is the fact that it allows for unsteady calculations even in the RANS limit. This is accomplished by the use of a time-accurate Navier-Stokes code and the use of a self-adjusting turbulence model (ASM). An example is provided in Figure 6 which shows perspective plots of the streamwise velocity

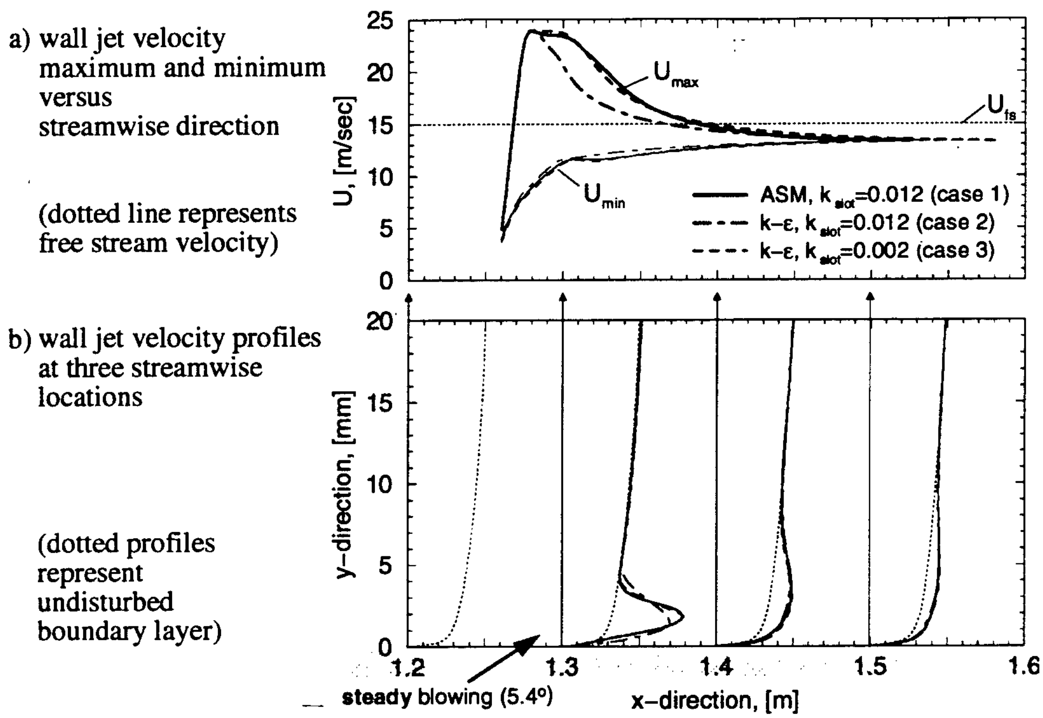

Figure 5: Test case for the new LES methodology: RANS calculation of a weak wall jet blown into a turbulent boundary layer through a slot at a shallow angle (5.4^o). Comparison of the streamwise velocity components computed with ASM and with a standard $k - \epsilon$ model.

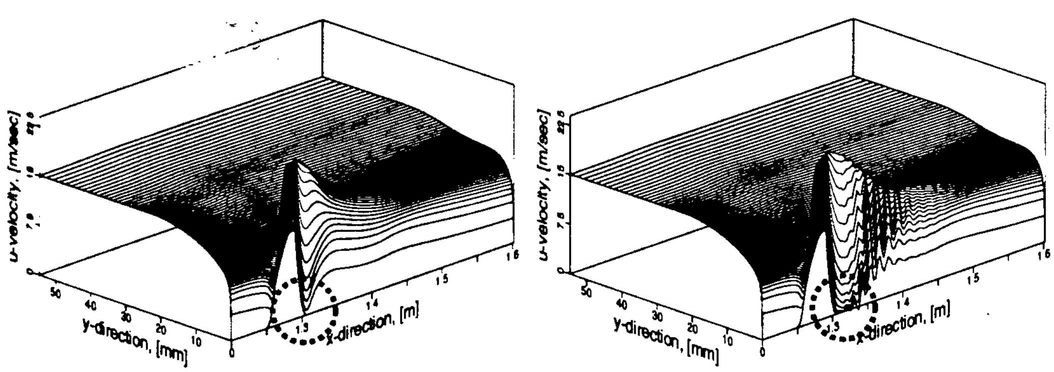

a) ASM, k_{slot}=0.012

b) ASM, k_{slot}=0.005

Figure 6: Unsteady RANS calculation of weak wall jet using ASM. Shown are perspective plots of the streamwise velocity for two different levels of turbulent kinetic energy that are specified over the blowing slot (k_{slot}).

for two RANS calculation using ASM with different levels of k_{slot}. While in the case of $k_{slot} = 0.012$ (Figure 6a) the flow converges to a steady state, in the the case of $k_{slot} = 0.002$ (Figure 6b), downstream traveling, unsteady structures are observed. These structures originate in a small separation bubble which has formed right downstream of the blowing slot. Note, that for smaller k_{slot} the jet has less turbulent intensity and, as a consequence, turbulent mixing is decreased. Therefore, locally the jet can separate from the surface. When the standard $k - \epsilon$ is used instead of the ASM, a separation bubble develops only for a much smaller k_{slot}, and even when vortical structures are eventually generated, they decay very rapidly.

4 LES using the Smagorinsky Model

In parallel with the development of our code employing the new LES methodology, we have investigated turbulent weak wall jets using LES with the Smagorinsky baseline model. While these simulations certainly could not capture all aspects of the complex flow correctly in a quantitative sense, they provided us with valuable reference data for our FSM approach.

4.1 Zero Pressure Gradient Flow

The weak wall jets were generated by blowing through an angled slot in the wall into a developed flat-plate boundary layer with zero free stream pressure gradient. The boundary layer in these simulations closely matches the artificially thickened boundary layer in the experimental investigations of forced turbulent weak wall jets by Wygnanski and coworkers (see Weidemann, 1996). An impression of the overall flowfield computed with our simulations is obtained from Figure 7, in which greyscales of instantaneous spanwise vorticity are displayed. In the simulation, a laminar boundary layer is tripped by 3D random blowing and suction through a slot close to the inflow (Figure 7). Further downstream, the weak wall jet is generated by tangential blowing

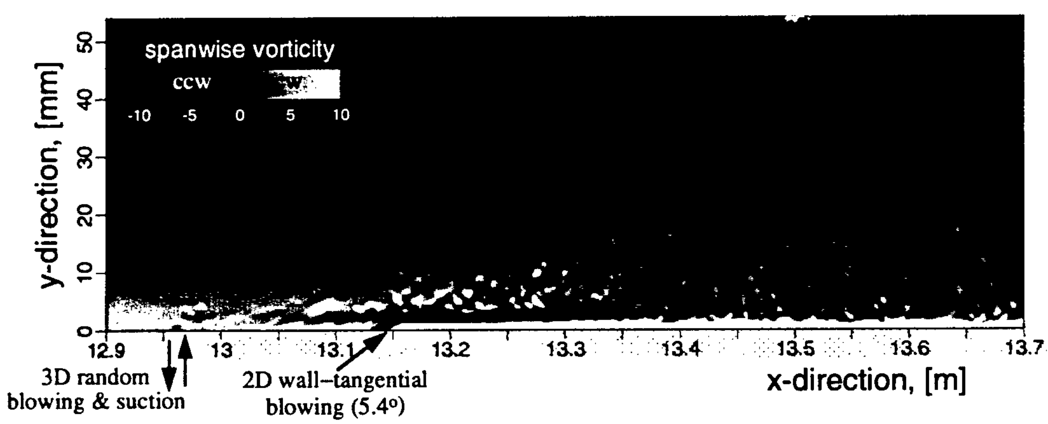

Figure 7: LES of a weak wall jet generated by tangential blowing through a slot in the wall into a turbulent boundary layer. Shown are greyscales of the 2D Fourier component of the instantaneous spanwise vorticity.

(angle 5.4^{o}) into the transitioning boundary layer through a second slot. In agreement with the experiments the jet persists for some streamwise distance ($\approx 25cm$) and then disintegrates.

The streamwise development of this weak wall jet can be nicely observed from the time-averaged streamwise velocity component, as illustrated in Figure 8 using perspective plotting. The velocity maximum of the wall jet decays rapidly and disappears about 25cm downstream of the slot. For comparison, the boundary layer without a wall jet is shown in Figure 8a. In the fully turbulent regime close to the outflow, the velocity profiles in Figures 8a and 8b are virtually identical. Results from other simulations, for which the wall jet was injected either farther upstream or farther downstream compared to the case of Figure 8b, are shown in Figures 8c and 8d. These results indicate that weak wall jets that are either generated in the regime of early transition (Figure 8c) or in the fully turbulent regime (Figure 8d) persist noticeably longer ($\approx 35cm$). The faster decay for the case in Figure 8b is probably due to the fact that the fluctuations in the flow are strongest during the later stages of transition. The destructive effect of large fluctuations on a weak wall jet were also observed in earlier simulations (Wernz and Fasel, 1997) where we attempted to generate a turbulent weak wall jet by tripping a laminar weak wall jet. As an example from these simulations, in Figure 9 corresponding perspective plots of the streamwise velocity are shown for the initial laminar weak wall jet and the transitional weak wall jet. While the unforced laminar weak wall jet persists throughout the computational domain (Figure 9a), when forced by 3D random blowing and suction, the wall jet decays rapidly as it transitions (Figure 9b).

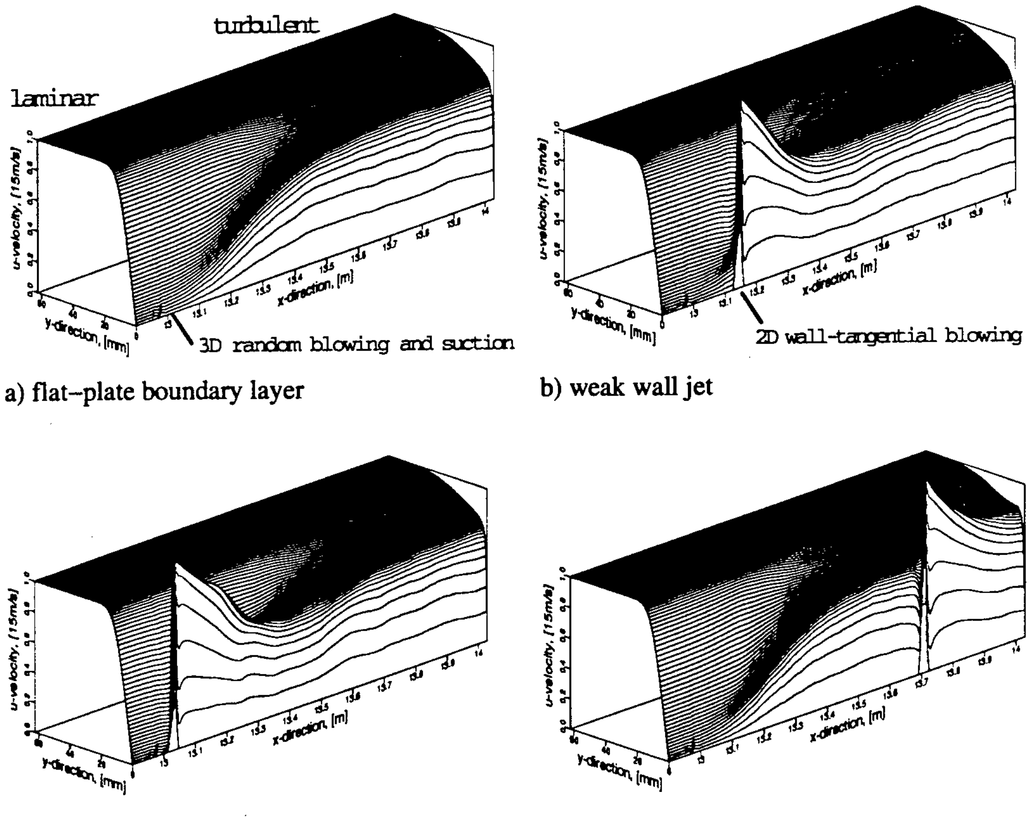

a) flat–plate boundary layer

b) weak wall jet

c) weak wall jet generated farther upstream

d) weak wall jet generated farther downstream

Figure 8: Comparison of weak wall jets generated by wall-tangential blowing through a slot at various downstream locations. Shown are perspective plots of the time-averaged streamwise velocity component (steady mean flow).

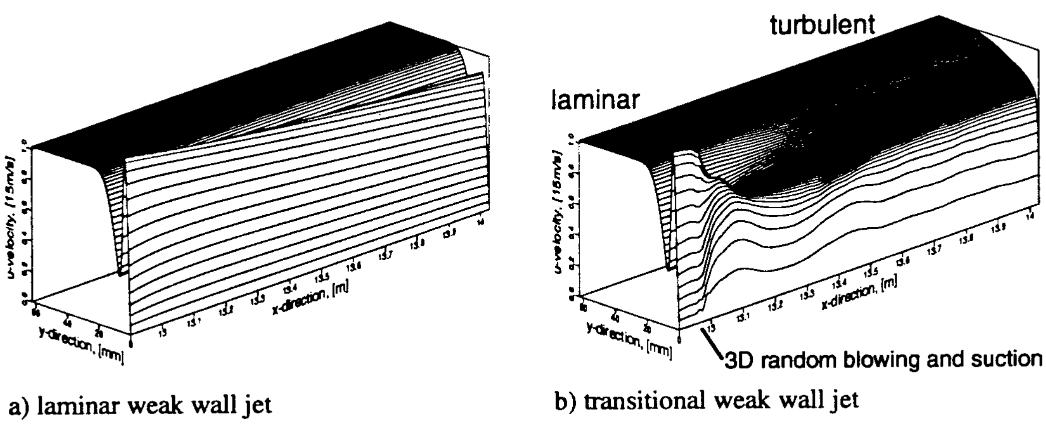

a) laminar weak wall jet

b) transitional weak wall jet

Figure 9: Comparison of a laminar and a transitional weak wall jet. Shown are perspective plots of the time-averaged streamwise velocity component (steady mean flow).

4.2 Adverse Pressure Gradient Flow

Towards the goal of investigating tangential blowing as a tool for separation prevention on an airfoil geometry, we have studied the effect of tangential blowing into a turbulent boundary layer with an adverse pressure gradient. A typical case of such investigations is presented in Figure 10. In the absence of blowing, the turbulent boundary layer separates due to the strong adverse pressure gradient, as illustrated in Figure 10a. When steady blowing is employed (Figure 10b), the flow remains attached, although it gets close to separation. With additional periodic forcing (Figure 10c) the flow does not come close to separation. This can be seen most clearly from the skin-friction coefficient plotted in Figure 10 for the three cases. While forcing the weak wall jet clearly produces two-dimensional coherent structures (Figure 10c), their growth rate is lower than could be expected from experimental findings (Zhou, personal communication). We suspect that the baseline Smagorinsky model, which was employed in this LES, provided too much dissipation and artificially dampens the coherent structures. Also, with the computational resources at our disposal, we were unable to provide sufficient resolution for the near-wall region.

Thus, for detailed investigation of the forced flow, there is a clear need for an improved modeling approach that does not artificially dampen out the coherent structures in the flow and is efficient enough to allow for parameter studies with a moderate computational expense.

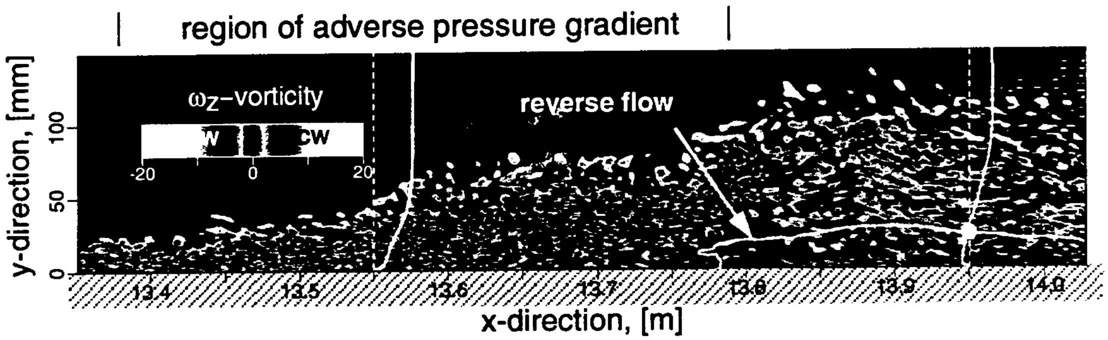

a) turbulent boundary layer without wall jet

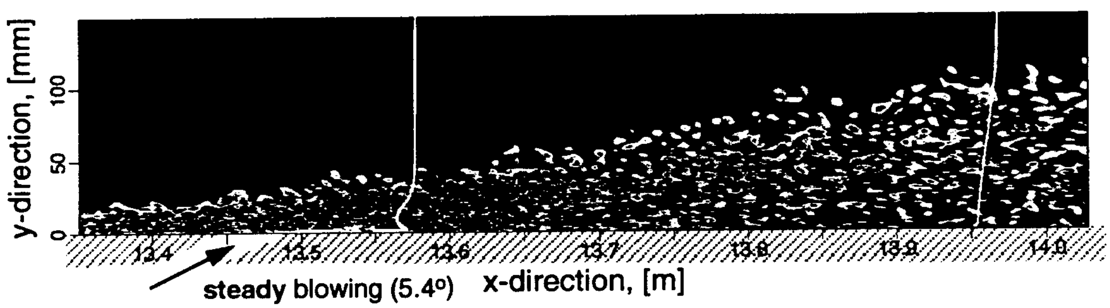

b) turbulent boundary layer with unforced wall jet

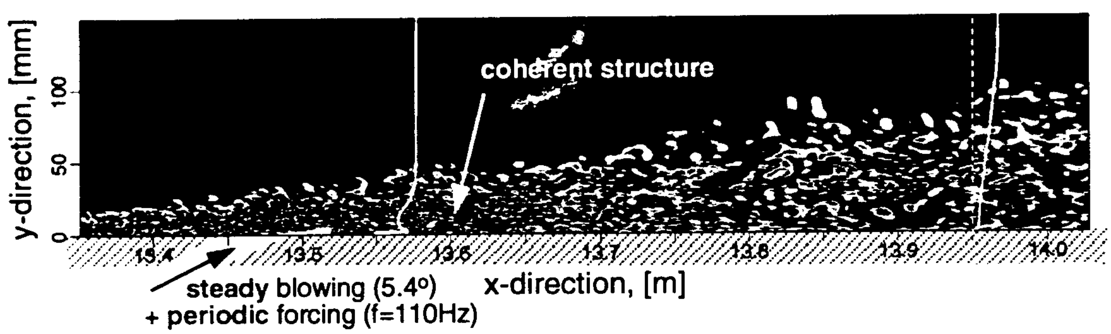

c) turbulent boundary layer with forced wall jet

Figure 10: Turbulent flat-plate boundary layer subjected to strong adverse pressure gradient. Separation prevention using a weak wall jet. Shown are color-contours for the 2-D Fourier component of the instantaneous spanwise vorticity.

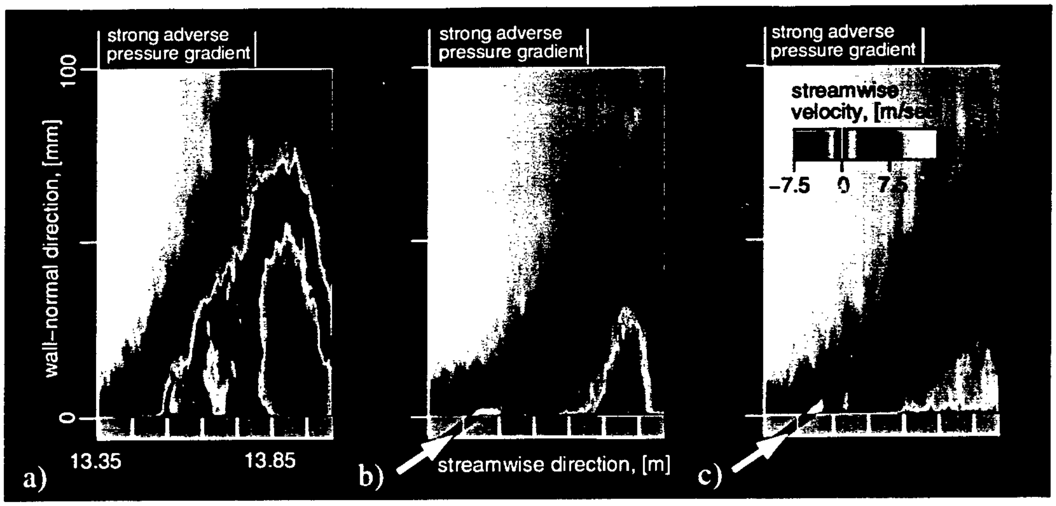

Figure 11: Color-contours for the 2-D Fourier component of the instantaneous streamwise velocity for the three cases shown in Figure 10.

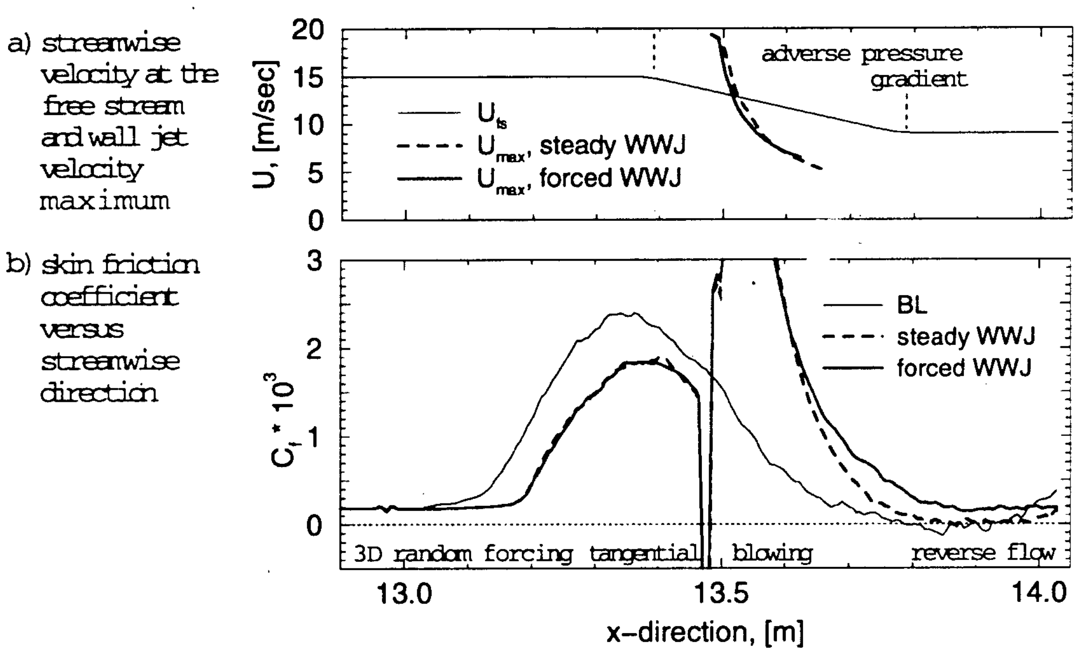

Figure 12: Streamwise development of time-averaged flow quantities for the three cases shown in Figure 10.

5 RANS Calculations

The objective of our two-dimensional RANS calculations is to investigate the generation and evolution of two-dimensional coherent structures in the weak wall jet at a fraction of the computational and logistical cost of three-dimensional LES and DNS. Results for a zero pressure gradient weak wall jet which approximately matches an experiment by Weidemann (1996) will now be discussed. The strategy for computing turbulent weak wall jets using RANS follows the approach taken for our LES (see section 4). A turbulent boundary layer is computed first, then the wall jet is generated by wall-tangential blowing through a slot. For the RANS calculations presented here, the Reynolds number is $Re_\theta = 2430$ at the inflow. [2] The Reynolds number at the blowing slot, $Re_\theta = 3420$, and the wall blowing parameters (steady blowing velocity $A_s = 1.3 \cdot U_{fs} = 19.5m/s$, blowing angle $\alpha = 5.4^o$) match those in the LES.

5.1 Steady RANS Calculations of the Unforced Flow

With our RANS calculations we can meet the grid resolution requirements for accurately computing weak wall jets. Results from a resolution study for the steady flow are presented in Figure 13. Three grid resolutions are considered, the lowest for base flow 1, the highest for base flow 3. The streamwise stepsize for base flows 2 and 3 matches that of the LES, for base flow 1 it is five times larger than for the LES. In wall-normal direction, base flow 1 has the resolution used in the LES, base flow 2 has twice and base flow 3 three times that resolution. In Figure 13a, the streamwise velocity profiles for the three base flows and for the turbulent boundary layer are plotted for three downstream locations. Overlayed are the locations of the jet velocity maximum U_{max} and the velocity minimum U_{min}. The jet extends to about $150mm$ downstream from the center of the blowing slot. Farther downstream, the

[2] In section 3.1 mean flow data close to the inflow are compared with experimental and DNS results.

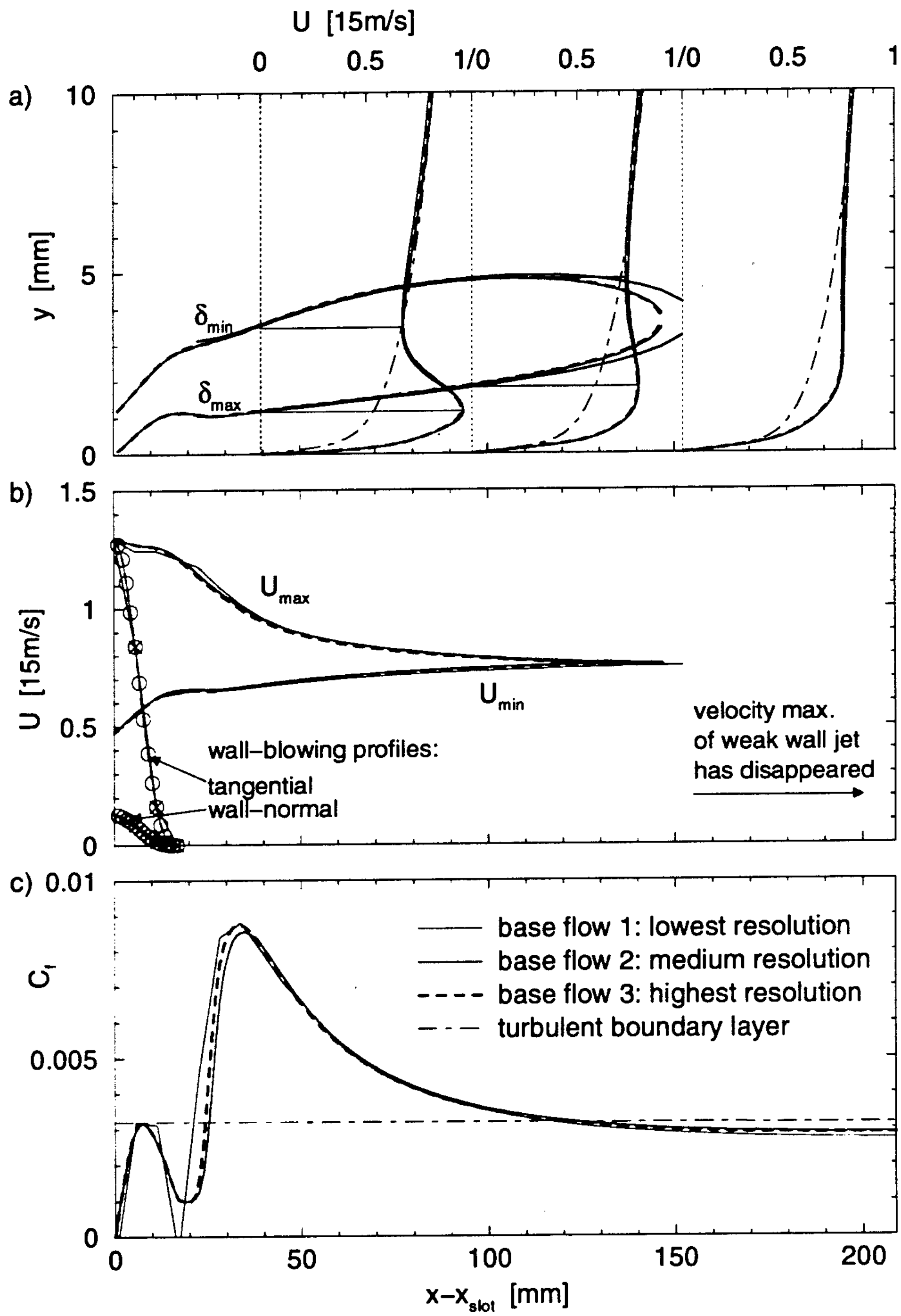

Figure 13: RANS calculation of steady weak wall jet. Shown are for three different grid resolutions: a) streamwise velocity profiles at three streamwise locations plus the wall-normal location of velocity maximum and minimum, b) wall-normal maximum and minimum of streamwise velocity, c) skin friction coefficient.

velocity maximum and minimum have disappeared, but a distortion of the boundary layer still persists. Figure 13b displays the streamwise development of the velocity maximum and minimum and Figure 13c shows the skin friction coefficient. For all quantities shown in Figure 13a-c, base flows 2 and 3 match closely, while base flow 1 deviates slightly, particularly for the skin friction close to the blowing slot. This is because the blowing slot is not well resolved with only five grid points (see Figure 15b).

In conclusion, for the steady flow the resolution used for base flow 2 is the best choice, the higher wall-normal resolution for base flow 3 is unnecessary. While the resolution for base flow 1 is adequate for steady flow calculations, this is not the case when computing the forced flow using URANS (see below).

5.2 Unsteady RANS Calculations of the Forced Flow

As a first step for gaining insight into the instability mechanisms of a weak wall jet we have recomputed a pulsed wall jet flow with URANS using the same forcing parameters as for the LES in section 4. For this case (denoted as case 1L), the forcing amplitude is very large, $A_p = 0.65 \cdot U_{fs}$, which is 50% of the steady blowing amplitude. A forcing frequency of $f = 110.8Hz$ is used. The URANS calculation was performed for the three base flows discussed above in section 5.1. Figure 14 illustrates the resulting flowfield for base flow 1 with color contours of instantaneous spanwise

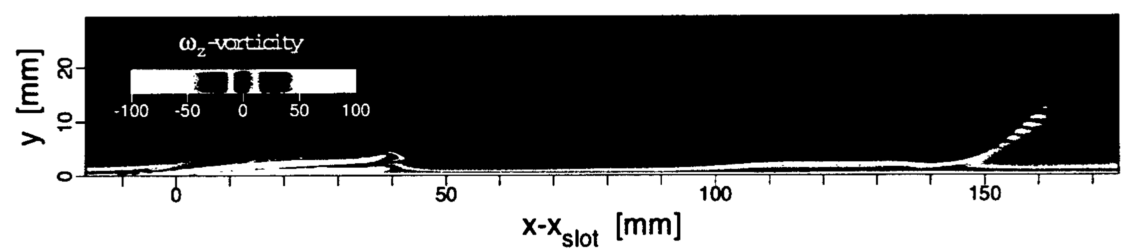

Figure 14: URANS calculation of a pulsed weak wall jet (base flow 1, medium grid resolution). Shown are color contours of instantaneous spanwise vorticity for case 1L.

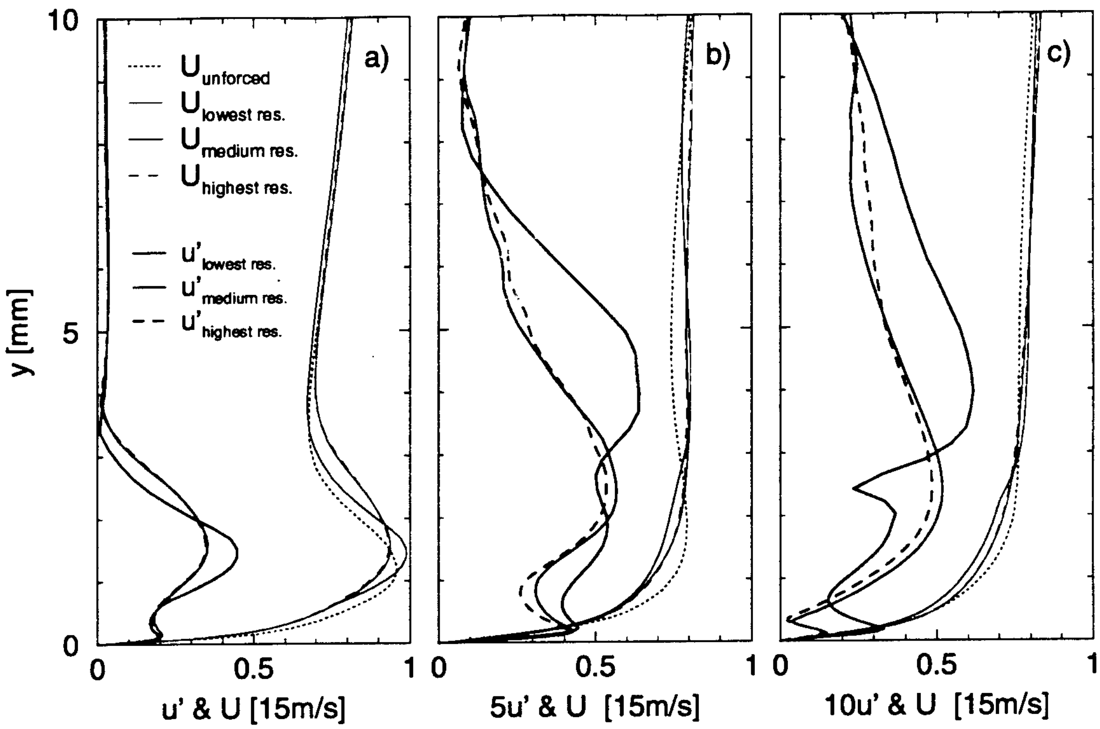

Figure 15: URANS calculation of pulsed weak wall jet, (case 1L— steady blowing with $A_s = 1.3U_{fs}$, pulsed blowing with $A_p = 0.65U_{fs}, f = 110.8Hz$). Shown are for three grid resolutions the streamwise mean flow profiles of the unforced and forced flow, and the Fourier amplitudes of the streamwise disturbances. The profiles are plotted for three streamwise locations (a-c) corresponding to those in Figure 13a.

vorticity. At this particular time instant, one localized dipolar structure can be observed $150mm$ downstream of the slot. The subsequent structure at $40mm$ is in the process of formation. Due to the large forcing amplitude, the resulting disturbances are highly nonlinear with localized vortical structures. For base flows 2 and 3, the streamwise resolution provides ten grid points for resolving these localized structures, while base flow 1 only provides two, which is clearly inadequate.

Consequently, as shown in Figure 15, the fundamental disturbance amplitudes from the URANS calculation with base flow 1 strongly deviate from those from calculations with base flows 2 and 3. Figure 15 also indicates that the disturbances are strongly damped. The disturbance amplitudes in Figure 15c are one order of magnitude lower than in Figure 15a. This is not really surprising for two reasons. Firstly, any nonlinear disturbance will decay if forced at an amplitude that is larger than its natural nonlinear saturation level, even if it is strongly amplified for smaller forcing amplitudes. Secondly, the large spacing between the localized disturbance structures shown in Figure 14, indicates that a forcing frequency of $f = 110.8Hz$ may be far too low for allowing amplified disturbances. From our experience with strong wall jets, vortical disturbances are strongly damped if the wave length is much larger than the local length scale which, in the present case, is the wall jet thickness characterized either by δ_{min} or δ_{max}. In addition, the wall jet mean flow decays drastically over one fundamental disturbance wave length and the shape of the weak wall jet profile with its three inflection points, (one at the wall, one in each free shear layer) are essential for the growth of two-dimensional disturbances. We therefore suspected that amplified disturbances exist for higher forcing frequencies where the wave length is in the order of the wall jet thickness. Therefore, we performed a parameter study to test this hypothesis.

From this parameter study, results of four cases are now presented. For all cases (case 1-4), the forcing amplitude was chosen as $A_p = 0.065 \cdot U_{fs}$ which is 5% of the steady blowing amplitude and ten times lower than that of the highly nonlinear forcing discussed above (case 1L). This should still be small enough to allow for disturbance growth before nonlinear saturation sets in. Figure 16 illustrates the four cases with color contour plots of instantaneous spanwise vorticity. From case to case, the forcing frequency is increased as indicated in the figure captions. For case 1, with the lowest frequency (Figure 16a), no vortical structures are discernible. The forcing frequency matches that of case 1L (Figure 14), but for the lower forcing amplitude used in case 1, the higher harmonics have a much lower amplitude and the disturbance is not localized. As the forcing frequency is increased (Figures 16b-d), vortical structures become visible. They appear strongest for case 3 in Figure 16c. As expected from the decay of the mean flow, the disturbances eventually decay for all cases.

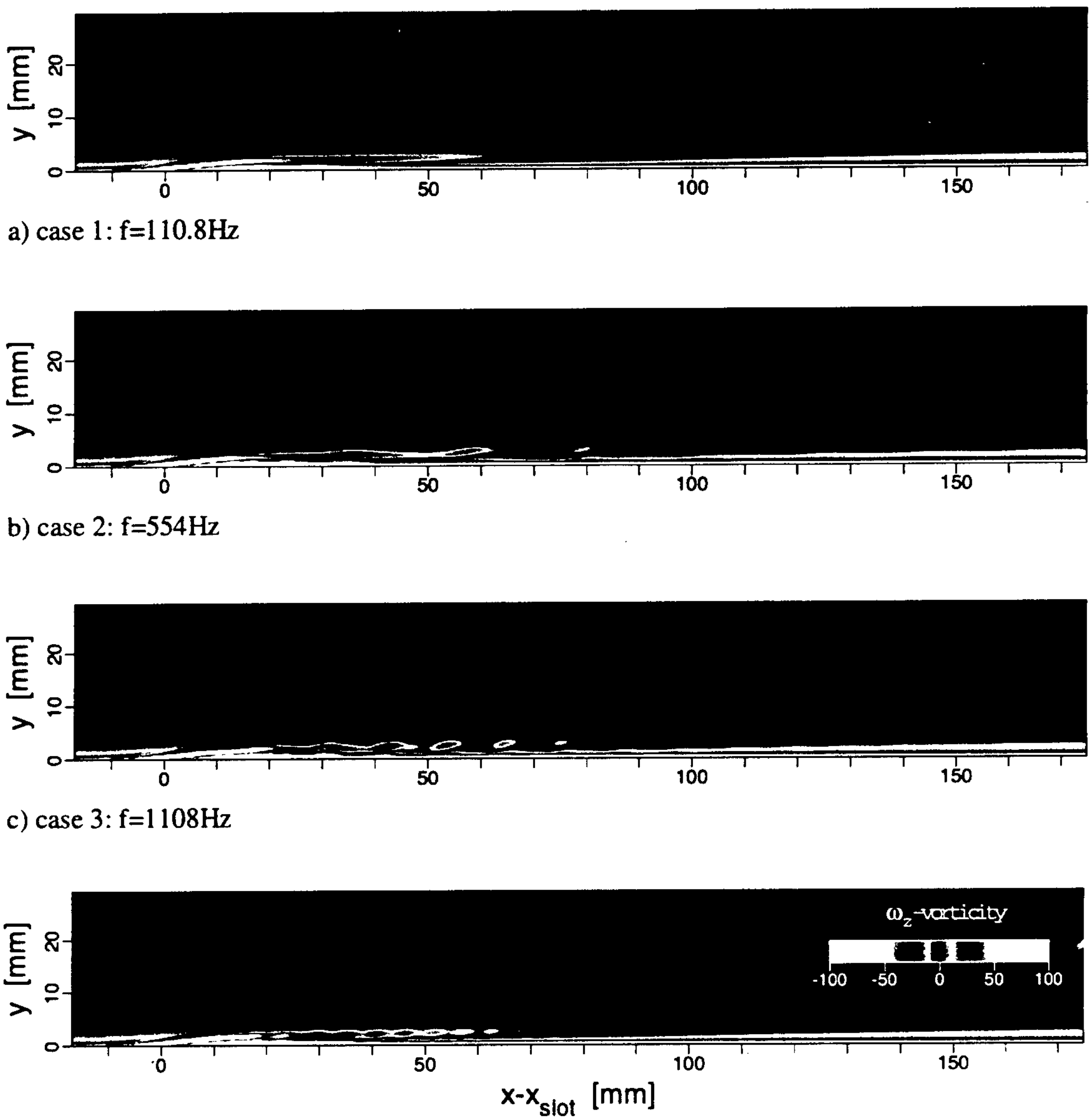

a) case 1: f=110.8Hz

b) case 2: f=554Hz

c) case 3: f=1108Hz

d) case 4: f=2216Hz

Figure 16: URANS calculations of pulsed weak wall jet (medium grid resolution). Shown are color contours of instantaneous spanwise vorticity for three different forcing frequencies. For all cases, steady wall-tangential blowing occurs with $A_s = 1.3 \cdot U_{fs}$, pulsed blowing occurs with $A_s = 0.065 \cdot U_{fs}$ while the forcing frequency varies as indicated.

A more detailed analysis of the magnitude of the disturbances and their streamwise amplitude development is presented in Figure 17. Shown for all four cases are three characteristic measures of the disturbances versus distance from the center of the blowing slot. Figure 17a depicts the fundamental wave length of the disturbances in comparison with the wall jet thicknesses, δ_{max} and δ_{min}. Once traveling disturbances establish shortly downstream of the blowing slot, their wave lengths stay fairly constant for all cases. The wave length for case 3 is about twice δ_{min}, while for case 4 it approaches δ_{min}. The decrease in wave length from case to case directly correlate with the increase in the forcing frequency, which indicates that they all travel at about the same phase speed.

The phase speed of the disturbances is shown in Figure 17b in comparison with the maximum and minimum velocity of the wall jet mean flow, U_{max} and U_{min}. For cases 2-4, the phase speed lies in between U_{max} and U_{min} while for case 1 it is at or above U_{max}. The disturbance for case 1 therefore decays, while growth is possible for cases 2-4. The phase speed of $\approx 0.8 \cdot U_{fs}$ also indicates that the disturbances are connected with an instability of the free shear layer, since boundary layer instabilities generally travel at lower speeds.

Finally, Figure 17c shows the amplitude maximum of the fundamental disturbance on a semi-logarithmic scale. The disturbance for case 1 indeed decays monotonically, while for cases 2 and 3 initial growth is observed, although not very strong and not for long. Interestingly, farther downstream the high frequency forcing cases 2-4 exhibit stronger decay than the low frequency case 1.

In Figure 18, the normalized shape of the disturbance amplitudes are plotted for three streamwise locations. For all disturbances, the largest amplitude peak is in the free shear layer of the wall jet, clearly indicating its connection with that portion of the flow profile.

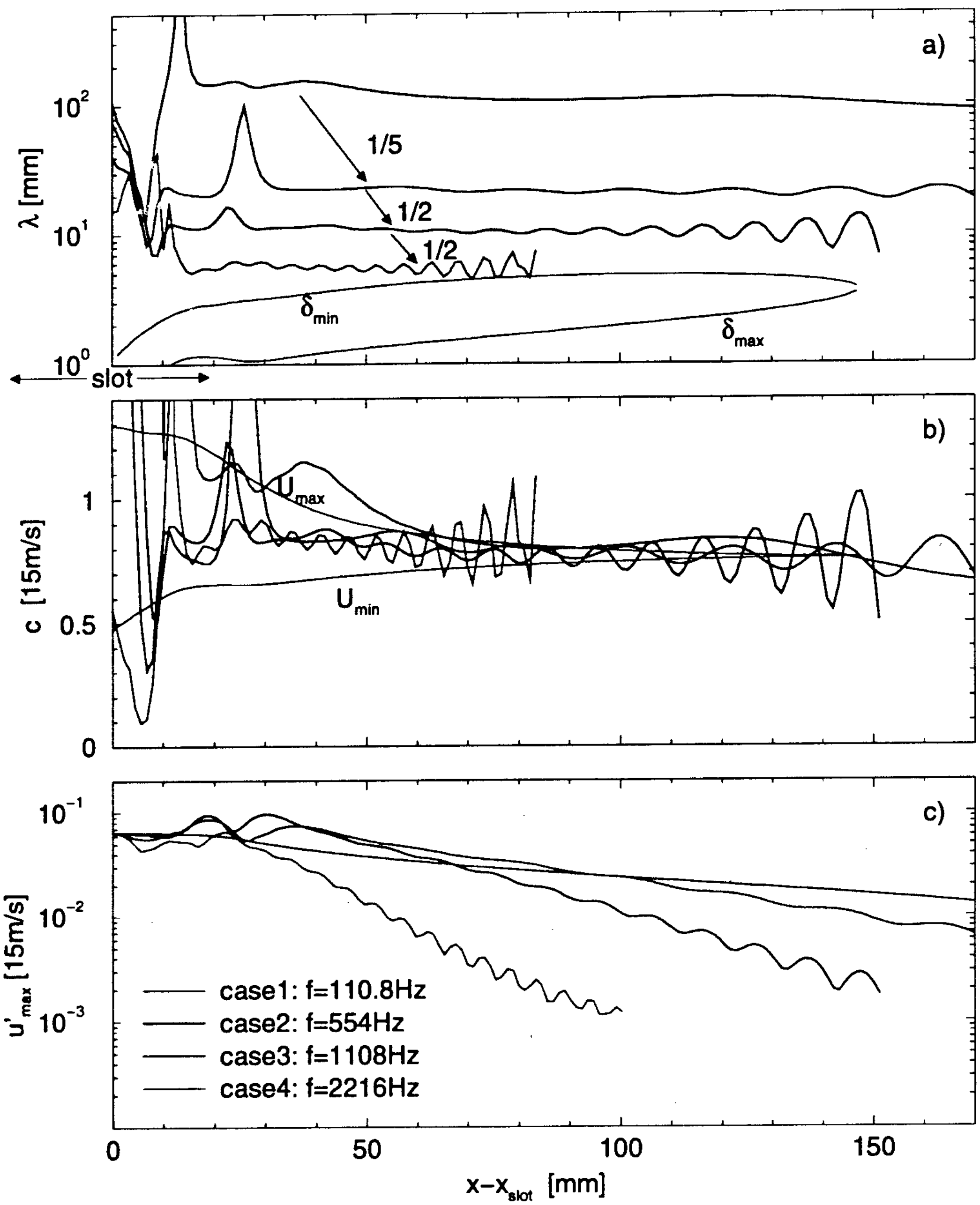

Figure 17: URANS calculations of pulsed weak wall jet, cases 1-4 (see Figure 16a-d). Shown are a) wave length, b) phase speed, and c) amplitude of the disturbances versus distance from the blowing slot.

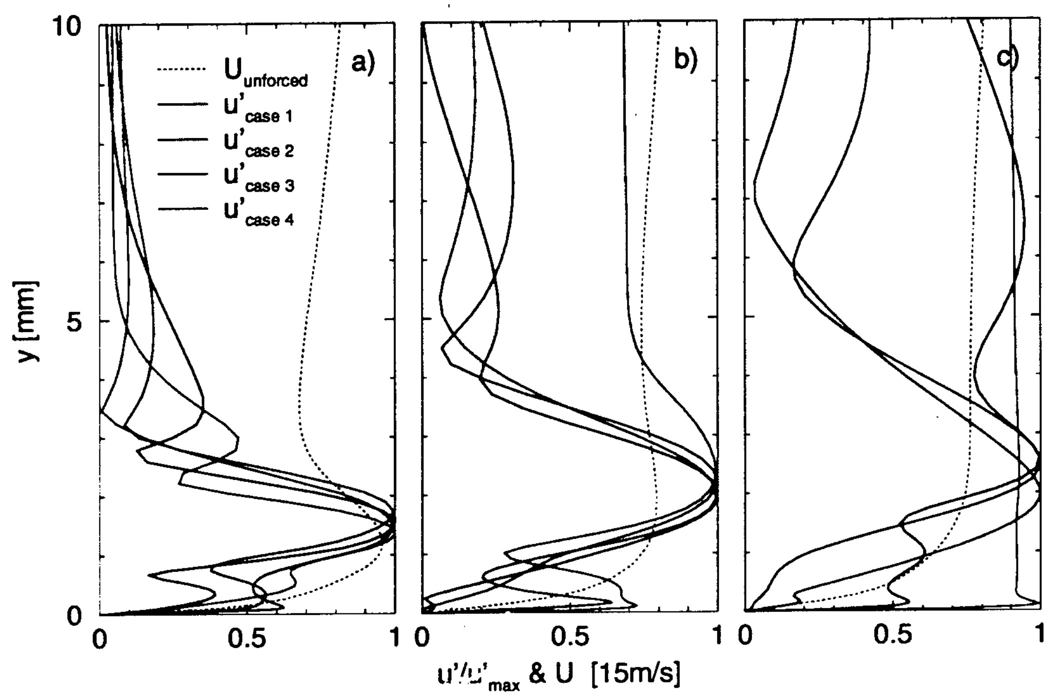

Figure 18: URANS calculations of pulsed weak wall jet, cases 1-4 (see Figure 16a-d). Shown are the Fourier amplitudes of the streamwise disturbances at three streamwise locations (a-c) corresponding to those in Figure 13a.

6 Summary and Outlook

With the present research we have successfully demonstrated that the problem of separation control using wall tangential blowing can be tackled with LES, DNS and a new Flow Simulation Methodology (FSM). Preliminary calculations using a conventional LES have shown that wall blowing is beneficial for delaying boundary layer separation. The calculations also indicated that pulsed blowing is more effective than steady blowing. In the LES, the pulsed blowing lead to the formation of 2D coherent structures. However, details of the formation process, the evolution of these structures, and the mechanism for delaying separation could not be determined with confidence, since the calculations lacked the proper resolution. The appropriate grid resolution for the LES would have been beyond the capacity of the available computational resources.

A very promising alternative to 3D LES are our FSM calculations in the 2D URANS limit. This approach was proven to be extremely successful, when applied to the benchmark case of a strong turbulent wall jet and yielded remarkable agreement with the experimental results. Since URANS calculations are two-dimensional, they are much less expensive than LES or DNS, and a much highe. wall-normal resolution can be afforded. For the unsteady weak wall jet, this enables to resolve the coherent structures well and to obtain the true shape of the amplitude distributions ("eigenfunctions"). We have started with parameter studies for a weak wall jet that is close to experiments by Wygnanski and coworkers. Our initial results from these URANS calculations are very encouraging. We could demonstrate that vortical disturbance can be generated with our approach. For smaller forcing amplitudes and within a certain frequency range, disturbance growth could be observed, even though only for a short distance. For large amplitude pulsing, low frequency forcing may prove to be the better choice, since the disturbances decay slower than for higher frequencies.

Many open questions remain, however. For example, from our investigations it is still unclear at present, whether the weak wall jet allows for subharmonic resonance. This is a prominent mechanism in transitional and turbulent strong wall jets and produces far greater growth rates than primary instability (see appendix). Potentially, a subharmonic cascade could be very helpful in naturally sustaining large coherent structures in the flow. A second issue which deserves further study is the receptivity problem. So far, from the many possible forcing methods, only longitudinal pulsing of the slot velocity has been employed which resulted in a shear layer mode of instability. With a more localized forcing method (e.g. applying a local force field inside the flow), different instability modes could be excited depending on the location of the forcing. For these detailed future investigations, a more realistic modeling of the slot geometry is clearly desirable. This is a very difficult problem, however, since "real" blowing slots in experiments and in technical wall jet applications may produce transitional, not fully turbulent flow. In general, it is extremely difficult to achieve a good match with experiments, because of the enormous set of parameters that can influence the wall jet flow, and which may not always be readily available.

References

Eriksson, J.G., Karlsson, R., I., and Persson, J., 1998, "An Experimental Study of a Two-Dimensional Plane Turbulent Wall Jet," *Exp. in Fluids* **25**, 50-60.

Fasel, H.F., Meitz, H.L., and Bachmann, C.R., 1997, "DNS and LES for Investigating Transition and Transition Control", AIAA Paper 97-1820.

Gatski, T. and Speziale, C., 1993, "On Explicit Algebraic Stress Models for Complex Turbulent Flows," *J. Fluid Mech.* **254**, 59-78.

Karlsson, R. I. and Johansson, T. G., 1988, "LDV measurements of higher order moments of velocity fluctuations in a turbulent boundary layer", in *Laser Anemometry in Fluid Mechanics*, D. F. G. Durao et al. (eds.), Portugal, Ladoan-Instituto Superior Tecnico, 273-289.

Meitz, H.L. and Fasel, H.F., 2000, "A Compact-Difference Scheme for the Navier-Stokes Equations in Vorticity-Velocity Formulation," *J. Comp. Phys.*, **157**, 3721-403.

Myong, H. K. and Kasagi, N., 1990, "A New Approach to the Improvement of the $k - \epsilon$ Turbulence Model for Wall Bounded Shear Flows," *JSME Int. J.*, **33**, 63-72.

Seidel, J., and Fasel, H., 2000, "Numerical Investigation of Forced Turbulent Wall Jets," AIAA Paper 2000-2317.

Seifert, A., Bachar, T., Koss, D., Shepshelovich, M., and Wygnanski, I., 1993, "Oscillatory Blowing: A Tool to Delay Boundary-Layer Separation," *AIAA J.* **31**, 2052-2059.

Seifert, A., Darabi, A., Sokolov M., and Wygnanski, I., 1994, "The Use of Oscillatory Blowing for Managing the Flow Around a Slotted Airfoil at Low Reynolds Numbers," Euromech Colloquium 328, Management and Active Control of Turbulent Shear Flows, Technische Universität Berlin.

Spalart, P. R., 1988, "Direct Simulation of a Turbulent Boundary Layer of up to $Re_\theta = 1410$", *J. Fluid Mech.* **187**, 61-98.

Sarkar, A. and So, R. M. C., 1997, "A Critical Evaluation of Near-Wall Two-Equation Models Against Direct Numerical Simulation Data," *Int. J. Heat and Fluid Flow*, **18**, 197-208.

Speziale, C., 1998, "Turbulence Modeling for Time-Dependent RANS and VLES: A Review", *AIAA J.* **36**, 173-184.

Weidemann, M., 1996, "The Weak Wall Jet", *Thesis*, Technische Universität Berlin.

Wygnanski, I., 1997, " Boundary Layer and Flow Control by Periodic Addition of Momentum (invited)," AIAA Paper 97-2117.

Zhang, H.-L. and Fasel, H., 1999, "Direct Numerical Simulation of the Turbulent Flow over a Stratford Ramp", AIAA Paper 99-3359.

Zhang, H.-L., Bachman, C.R., and Fasel, H.F., 2000a, "Reynolds-Averaged Navier-Stokes Calculations of Unsteady Turbulent Flow," AIAA Paper 2000-0143.

Zhang, H.-L., Bachman, C.R., and Fasel, H.F., 2000b, "Application of a New Methodology for Simulations of Complex Turbulent Flows," AIAA Paper 2000-2535.

Presentations at Conferences

Wernz, S. and Fasel, H., 1997, "Numerical Investigation of Forced Strong and Weak Wall Jets," *APS*, 50th Annual Meeting of the Division of Fluid Mechanics, San Francisco, CA, November 23-25.

Wernz, S. and Fasel, H., 1999, "Numerical Investigation of Turbulent Weak Wall Jets Using LES and RANS," 15th Arizona Fluid Mechanics Conference, Tucson, AZ, April 23-24.

Wernz, S. and Fasel, H., 1999, "Numerical Investigation of Resonance Phenomena in Wall Jet Transition", IUTAM Symposium on Laminar-Turbulent Transition, Sedona, Az, September 13-17, 1999.

Seidel, J., and Fasel, H., 2000, "Numerical Investigation of Forced Turbulent Wall Jets," AIAA-Fluids 2000, Denver, Co, June 19-22.

APPENDIX

Paper presented at the IUTAM Symposium on Laminar-Turbulent Transition, Sedona, Az, September 13-17, 1999.

Numerical Investigation of Resonance Phenomena in Wall Jet Transition

Stefan Wernz and Hermann F. Fasel

The University of Arizona, PO Box 210119, Tucson, AZ 85721, USA

Abstract. The competition between 2-D and 3-D resonances in wall jet transition is analyzed using DNS. In 2-D DNS strong growth of subharmonic disturbances is observed which leads to a subharmonic resonance cascade. When a periodically forced flow is simultaneously perturbed by a small amplitude pulse, massive vortex ejections occur. With 3-D DNS it is shown that additional 3-D forcing can prevent vortex mergings and vortex ejections by reducing the spanwise coherence of the vortices, in particular close to the wall.

Key words: wall jet, subharmonic resonance, pulse disturbance, vortex ejection

1 Introduction

The transitional Glauert wall jet [2] is studied, because this flow geometry is prototypical for important technical applications, such as film-cooling and boundary layer control. While the Glauert wall jet is geometrically simpler than technical wall jet flows, it exhibits the same main characteristics, the presence of a boundary layer (near-wall region) in close proximity to a free shear layer (outer region). Due to the inflection point in the velocity profile, the outer region of the wall jet is susceptible to an inviscid Kelvin-Helmholtz type instability which may give rise to two-dimensional (2-D) subharmonic resonances. Due to the presence of the wall, the near-wall region is governed by viscous instability. Thus, growth of Tollmien-Schlichting type waves can occur allowing for three-dimensional (3-D) secondary instabilities (fundamental and subharmonic resonances). Therefore, in a wall jet 2-D and 3-D resonance mechanisms can exist simultaneously and may compete with each other. In fact, various transition scenarios have been observed in experiments of forced transitional wall jets. For example, in experiments by Bajura and Catalano [1], 2-D subharmonic resonance plays a major role during transition, whereas in experiments by Shih and Gogineni [4], three-dimensionality sets in immediately downstream of the primary disturbances. In previous work, using direct numerical simulations (DNS), we have investigated 2-D secondary instability [5] and 3-D secondary instabilities [6] separately. For the investigated cases, we concluded that 3-D subharmonic resonance is at least as strong as the 2-D subharmonic resonance. With the present study (also using DNS), transition scenarios are investigated where both 2-D and 3-D resonances occur simultaneously. Through selective forcing the conditions are explored under which 2-D resonances or 3-D resonances dominate the transition process.

2 Computational Approach

For the DNS, a 3-D incompressible Navier-Stokes code for DNS of boundary layer transition [3] has been adapted to the wall jet geometry. In the DNS the incompressible vorticity transport equations (VTE) and velocity Poisson equations are solved in total flow formulation inside the computational domain shown in Fig. 1. The numerical scheme employs a fourth-order accurate Runge-Kutta method for the time integration and fourth-order compact differences in streamwise and wall-normal directions. For the wall-normal direction a variable grid is used with points clustered

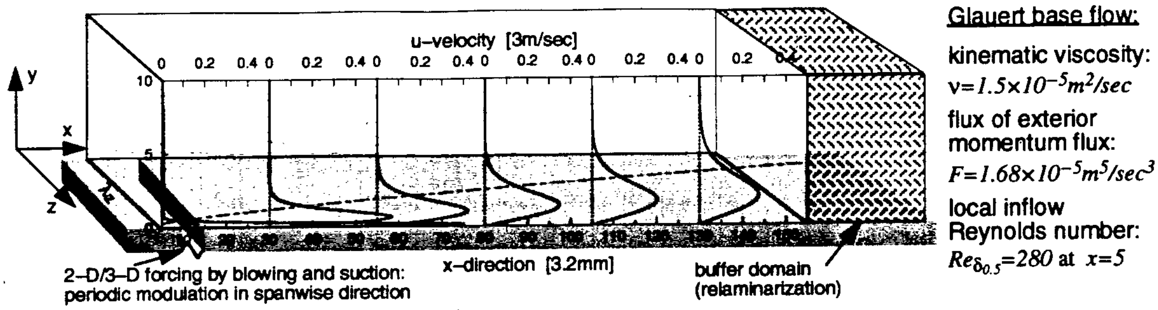

Figure 1: Computational domain with Glauert base flow and blowing/suction slot for disturbance generation

near the wall. In 3-D DNS the spanwise direction is treated pseudo-spectrally. The boundary conditions include Dirichlet conditions at the inflow, zero disturbances at the free stream boundary, and a buffer domain near the outflow boundary for relaminarizing the flow [3]. At the wall, the velocity is set to zero except over the blowing and suction slot. In a DNS precursor calculation, a 2-D base flow is computed (Fig. 1) which closely matches the simi- larity solution that was used in [5] as a base flow. To ensure that the DNS base flow is independent of the computational domain height, special care must be taken to recover the induced flow field of the wall jet far away from the wall, where the similarity solution is invalid. This is achieved by imposing flow profiles at the inflow that combine the similarity solution near the wall with an asymptotically matched potential flow solution away from the wall.

2.1 Forcing Method

For the transition simulations, the base flow is forced by simultaneous blowing and suction through a slot in the wall close to the inflow boundary. This technique is very efficient in producing vortical disturbances while minimizing acoustic disturbances. The slot velocity is computed as

$$v_s(x, y=0, z, t) = F_{v_s}(x) \cdot \sum_{k=0}^{K} \sum_{n=0}^{N} A_{(n,k)} \cdot \cos(2\pi f_n t) \cdot \cos(\gamma_k z) \qquad (14)$$

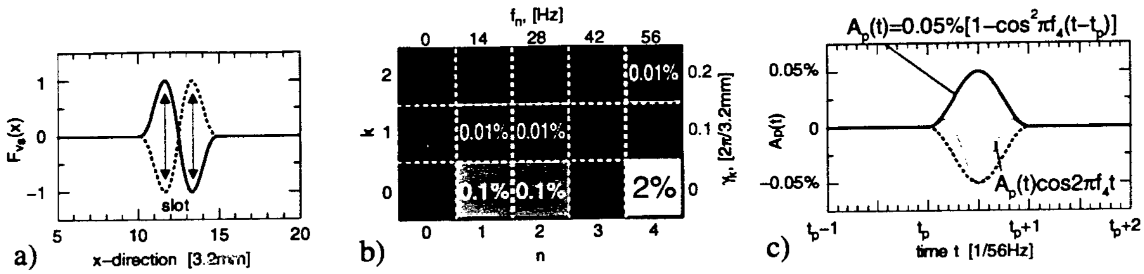

Figure 2: Forcing method **(a)** streamwise variation $F_{v_s}(x)$ **(b)** mode diagram for forcing amplitudes $A_{(n,k)}$ of periodic forcing **(c)** amplitude $A_p(t)$ of pulse disturbance

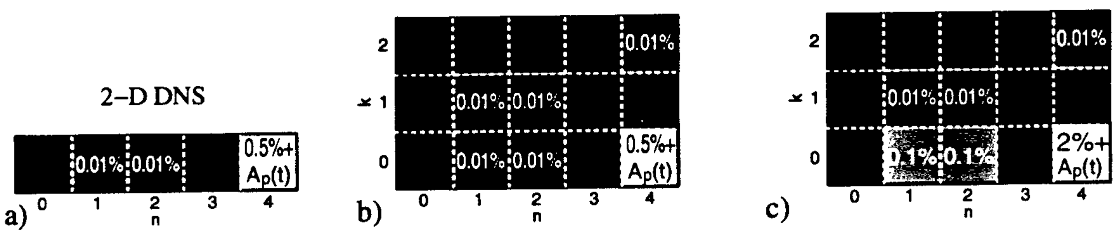

Figure 3: Mode diagrams for forcing amplitudes **(a)** Case 1 **(b)** Case 2 **(c)** Case 3

where $A_{(n,k)}$ is the forcing amplitude of mode (n, k) in [%], $f_n = n \cdot f$ is the frequency in $[Hz]$, $\gamma_k = k \cdot 2\pi/\lambda_z$ is the spanwise wave number in $[1/3.2mm]$. The forcing method is illustrated in Fig. 2. At first, the flow is forced periodically (Fig. 2b) until it converges to a time-periodic state. Then, at time t_p, a small pulse disturbance (Fig. 2c) is also introduced in mode $(4, 0)$. In the present paper, three cases with different periodic forcing are discussed (Fig. 3). The pulse disturbance (Fig. 2c) is identical for all cases.

2.2 Computational Parameters

The flow quantities are non-dimensionalized with a reference length, $L = 3.2mm$, and the base flow velocity at the slot, $U = 3m/sec$. For the discretization in streamwise direction, a constant stepsize, $\Delta x = 0.125L$, is employed for all cases. The domain length varies however: For Case 1, 1201 points (+ 800 points in buffer domain) are used. For Case 2, 1201 (+ 400) points are used, and for Case 3, 801 (+ 200) points. In wall-normal direction, an exponentially stretched grid with 180 points is employed where the smallest stepsize, $\Delta y_{min} = 0.02L$, is at the wall, and the largest stepsize, $\Delta y_{max} = 1.2L$, is at the upper boundary. The spanwise direction is composed of 11 symmetric spectral modes with the largest spanwise wave number $\gamma_1 = 0.1 \cdot 2\pi/L$.

2.3 Validation of Computations

For validation of the DNS code see Meitz [3]. For the DNS of wall jets, convergence investigations regarding the effect of stepsizes have ensured that the the influence of the discretization error on the flow solution is kept small. Especially for 2-D simulations, a long buffer domain is crucial for preventing upstream feed from the outflow boundary. Even small feed back can excite strongly amplified low frequency disturbances which can prevent the flow from reaching a time-periodic state.

3 Results

We have conducted numerical experiments to uncover the relative importance of 2-D and 3-D secondary instabilities. Three case studies are presented here.

3.1 2-D Flow – Case 1

In Case 1, the flow is forced with a fundamental and two subharmonic frequencies, all 2-D (Fig. 3a). The resulting time-periodic flow exhibits two subsequent vortex mergings (Fig. 4a). A Fourier decomposition of the time-periodic flow (Fig. 4b) reveals that, through resonance with the large fundamental disturbances, the small subharmonic disturbances are strongly amplified and successively surpass the amplitude of the fundamental. This subharmonic cascade is, however, extremely sensitive to small non-periodic disturbances.

When at time t_p the wall jet is additionally perturbed with a small pulse (Fig. 2c), it responds by ejecting dipolar vortices away from the wall (Fig. 5a) and, in fact completely lifts off from the wall. As illustrated in the $x - t$ diagram in Fig. 5b, the pulse disturbance generates a downstream traveling wave packet which grows in amplitude by two orders of magnitude and exhibits several doublings of the dominant wave length. In contrast, without the presence of large, periodic disturbances (not shown), the wave packet barely grows and experiences only a gradual shift to smaller

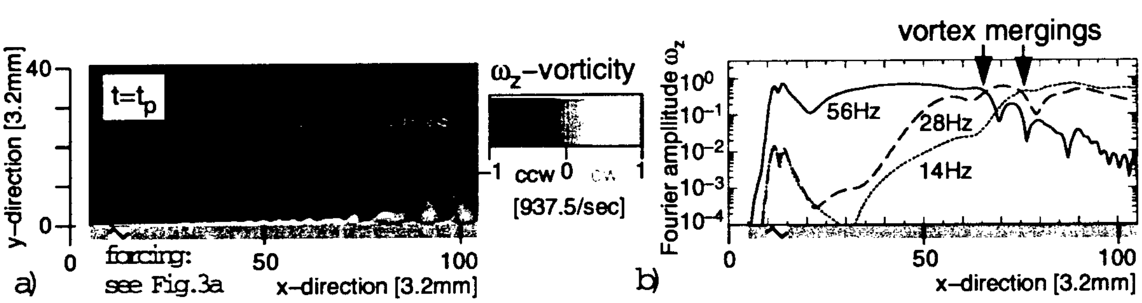

Figure 4: Time-periodic flow – Case 1 **(a)** grey scales of instantaneous ω_z-vorticity **(b)** Fourier amplitudes of ω_z-vorticity at $y = 0$ for three modes

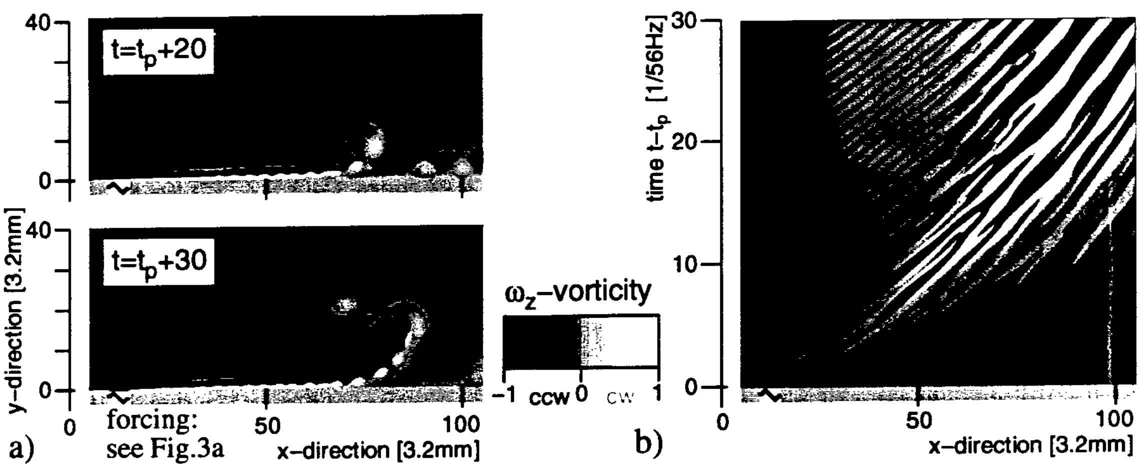

Figure 5: Flow response to small pulse disturbance – Case 1 **(a)** grey scales of ω_z-vorticity **(b)** x-t diagram of ω_z-vorticity at $y = 0$ (flow with pulse - without pulse)

wave numbers. This indicates that the subharmonic components in the wave packet are strongly amplified through resonance with the large amplitude periodic disturbances. As the wave packet reaches the amplitude level of the periodic disturbances it disrupts the balance of the double vortex row and causes the ejection of vortex pairs.

3.2 3-D Flow – Cases 2 and 3

For Case 2, in addition to the disturbances of Case 1, 3-D disturbances with the same amplitudes as the 2-D subharmonic disturbances are introduced (Fig. 3b). Now, the flow becomes highly three-dimensional downstream of $x = 70$. As illustrated in Fig. 6a, the same pulse as in Case 1 causes no vortex ejections, but merely produces a number of small vortices that linger in the outer region of the wall jet before they are convected out of the computational domain. How differently the wave packet now develops compared to Case 1 becomes evident from the $x - t$ diagrams for the two cases (Figs. 6b and 5b). Initially, both cases are virtually identical. But downstream of $x = 70$, where in Case 1 the vortex ejection occurs, in Case 2 the amplitude of the

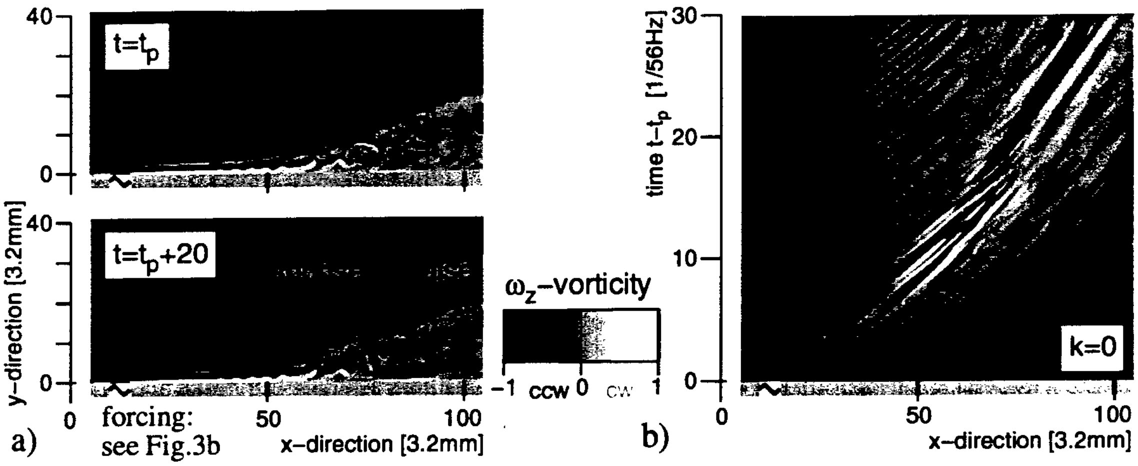

Figure 6: Flow response to small pulse – Case 2 (**a**) grey scales of ω_z-vorticity at $z = 0$ (**b**) x-t diagram of ω_z-vorticity for $y = 0$, $k = 0$ (with pulse - without pulse)

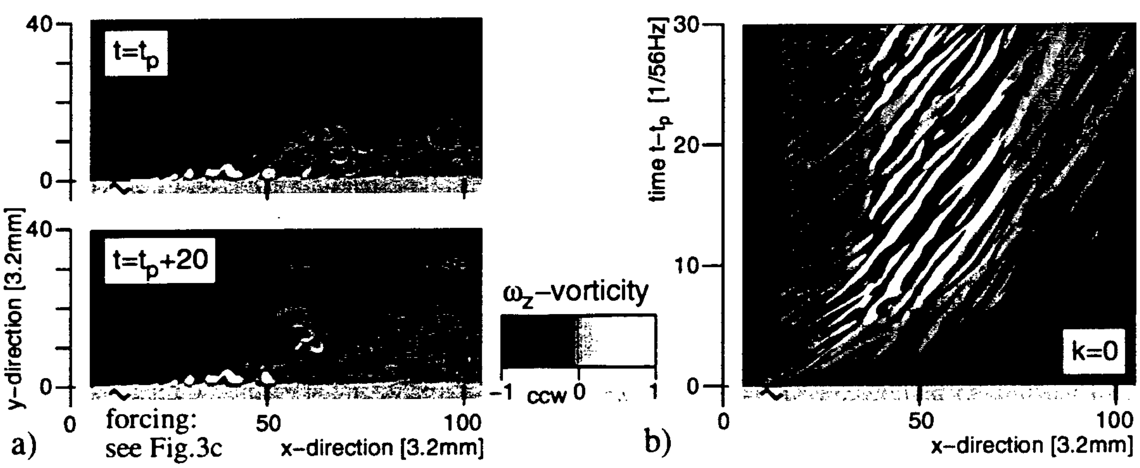

Figure 7: Flow response to small pulse – Case 3 (**a**) grey scales of ω_z-vorticity at $z = 0$ (**b**) x-t diagram of ω_z-vorticity for $y = 0$, $k = 0$ (with pulse - without pulse)

spectral component $k = 0$ of the wave packet decreases markedly. The wave packet looses its spanwise coherence along with the periodic 2-D disturbances.

Only when, as in Case 3, the amplitude of both the 2-D fundamental and subharmonic forcing is significantly increased (Fig. 3c), vortex merging and vortex ejection occur prior to development of the three-dimensional stage (Fig. 7a). Now the wave packet

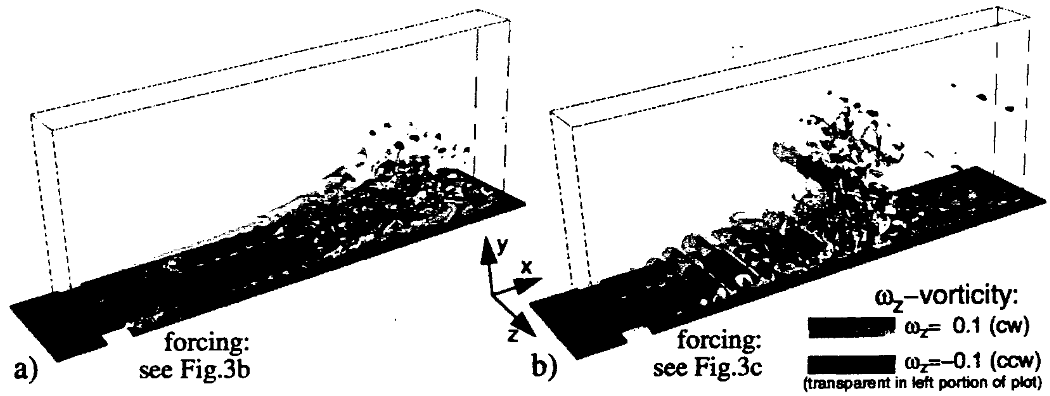

Figure 8: Flow response to small pulse disturbance. Shown are iso-surface plots of ω_z-vorticity at time $t = t_p + 30$ **(a)** Case 2 **(b)** Case 3.

reaches a large amplitude level and exhibits a doublings of the dominant wave length (Fig. 7b).

The difference in the transition process between Case 2 and Case 3 and the impact of the small pulse in each case is nicely illustrated by the 3-D snapshots in Fig. 8. While in Fig. 8a the flow becomes highly three-dimensional immediately downstream of the fundamental disturbance, in Fig. 8b vortex mergings and the ejection of a dipolar vortex precede the 3-D stages.

4 Conclusion

In our 2-D DNS of a forced wall jet, we found that subharmonic resonance is the dominant mechanism. It strongly amplifies small (subharmonic) disturbances and thus renders the flow extremely sensitive to small amplitude pulse (or random) disturbances causing vortex ejections and the possible disintegration of the wall jet. In our 3-D DNS, the 2-D subharmonic resonance may be surpassed by 3-D resonances which, as a consequence, inhibit vortex mergings and vortex ejections. Our findings may explain experimental observations, where vortex mergings and vortex ejections occur for low Reynolds numbers and low turbulence levels [1], but not for higher Reynolds numbers and higher turbulence levels [4].

This research was funded by AFOSR under Grant Number F49620-94-1-0208 and was also supported in part by a grant of HPC time from the DoD HPC Shared Resource Centers, ERDC and NAVO.

References

[1] Bajura, R. A. and Catalano, M. R. (1975) Transition in a Two-Dimensional Plane Wall Jet. *J. Fluid Mech.*, **70**:773–799

[2] Glauert, M. B. (1953) The Wall Jet. *J. Fluid Mech.*, **1**:625–643

[3] Meitz, H. and Fasel, H. F. (2000) A Compact-Difference Scheme for the Navier-Stokes Equations in Vorticity-Velocity Formulation. *J. Comp. Phys.*, **157**:371–403

[4] Shih, C. and Gogineni, S. (1995) Experimental Study of Perturbed Laminar Wall Jet. *AIAA J.*, **33**:559–561

[5] Wernz, S. and Fasel, H. F. (1996) Numerical Investigation of Unsteady Phenomena in Wall Jets. *AIAA Paper*, 96-0079

[6] Wernz, S. and Fasel, H. F. (1997) Numerical Investigation of Forced Transitional Wall Jets. *AIAA Paper*, 97-2022

NUMERICAL INVESTIGATION OF FORCED TURBULENT WALL JETS

J. Seidel[*], H. F. Fasel[†]
Department of Aerospace and Mechanical Engineering, University of Arizona
Tucson, Arizona, USA

Abstract

The effect of time periodic forcing of turbulent wall jets is investigated numerically using our new Flow Simulation Methodology (FSM). Previous experimental research has shown that periodic excitation of wall jets increases their effectiveness for separation control. To investigate the effect of forcing on the large coherent structures, a steady mean flow is computed first using a Reynolds Averaged Navier-Stokes (RANS) approach. The response of this mean flow to periodic forcing is then investigated using FSM in the limit of unsteady RANS. Our results indicate that with periodic forcing, significant changes in the mean Reynolds shear stress distribution and also the skin friction are observed. The unsteady computational results are scrutinized to investigate how the coherent structures interact with the turbulent mean flow and what role they play in the change of the mean flow profiles.

1 Introduction

A wall jet develops when a fluid is blown tangentially along a surface. Wall jets have many important technical applications such as boundary layer control and lift enhancement on airfoils, making use of their tendency to adhere to curved surfaces (Coanda effect). In other applications, such as the cooling of turbine blades and combustion chamber walls, a wall jet is used to cool and protect surfaces from hot and/or corrosive fluids.

Irrespective of its application, a wall jet acts as a source of momentum. The jet may be issued into a coflowing, quiescent, or counterflowing surrounding. The external stream may be accelerating or decelerating such as in airfoil or turbine blade applications. In addition, the external flow can be laminar or turbulent. The surface itself might be smooth, rough, or even highly irregular, such as in electronic cooling applications. Despite its applications in many technical systems, the wall jet, especially the role of large coherent structures in the turbulent wall jet, is not at all understood.

Experimental work by Wygnanski and coworkers [1] has demonstrated the effectiveness of using pulsed wall jets for delaying separation. Using flow visualization, Wygnanski was able to show large coherent structures in the turbulent flow on an airfoil. These structures profoundly affect the mean flow, significantly delaying separation. More importantly, deliberately introducing these structures using periodic forcing results in predictable changes of the mean flow.

The geometry used in the experiments is highly complex, combining the effects of wall curvature, adverse pressure gradient, a coflowing external stream, and unsteady momentum addition by the pulsed wall jet. To understand the most dominant physical mechanisms in this flow, it is paramount to understand the influence of every component of the flow in the experimental investigation. As a first step in a series of numerical investigations, the effect of periodic forcing on the turbulent mean flow of the strong turbulent wall jet on a flat surface is studied in this paper.

A large number of experimental investigations of the mean flow of turbulent wall jets has been reported in the literature (see review articles [2], [3], [4]). Although the measurements are very consistent in a large part of the mean profiles, the velocity in the near wall region is extraordinarily difficult to measure and therefore skin friction data vary considerably. Furthermore, since these experimental investigations focused on the mean flow quantities only, the question of the existence and influence of large coherent structures in the outer shear layer on the mean flow profiles was not addressed.

In this paper, the role of these large coherent structures is investigated numerically using our new Flow Simulation Methodology (FSM). This ap-

*Research Assistant. Member AIAA.
†Professor, Aerospace and Mechanical Engineering. Member AIAA.

proach has been developed in collaboration with C. Speziale [5] because of the limitations in traditional computational strategies such as Direct Numerical Simulation (DNS), Reynolds-averaged Navier-Stokes (RANS) computation, and Large Eddy Simulation (LES). DNS is limited to relatively low Reynolds number flows and is, in the foreseeable future, impractical for high Reynolds number flows which are of greatest engineering interest. This leaves Reynolds-averaged Navier-Stokes (RANS) calculations and Large-Eddy Simulation (LES) as the only realistic alternatives to compute turbulent flows [5]. However, traditional RANS methods are limited to time-steady solutions, an assumption unsuitable for complex turbulent flows where unsteady large structures play a dominant role in the transfer of heat and momentum between different regions of the flow. From a theoretical standpoint, LES has long been viewed as an ideal method for the time-dependent, spatially varying solution of complex turbulent flows. Unfortunately, the promise of LES to provide reasonable solutions for larger Reynolds numbers remains largely unfulfilled.

FSM is aimed at combining the advantages of RANS and LES in a consistent manner. In fact, FSM maintains the general form of LES, i.e., the large scales are computed and the small scales are modelled. The main feature of our FSM is that the subgrid-scale stress model of LES is replaced by the product of a contribution function and a state-of-the-art Reynolds stress model. The contribution function is designed such that, depending on the numerical resolution (as compared to a turbulent length scale like the Kolmogorov length scale), the simulations approach a DNS in the limit of fine resolution (or low Reynolds number), or an unsteady RANS in the limit of coarse resolution (or high Reynolds number).

Using FSM in the unsteady RANS limit, the role of the large coherent structures in the turbulent wall jet is investigated in this paper. Experimental investigations ([6], [7]) have shown that the skin friction is markedly reduced when large amplitude disturbances are introduced into the turbulent wall jet. Furthermore, the experiments by Schober [8] show that the resulting coherent structures are predominantly two-dimensional. If these structures are in fact two-dimensional, a two-dimensional simulation in the FSM limit of unsteady RANS should be able to capture the most important effects of the coherent motion on the turbulent mean flow.

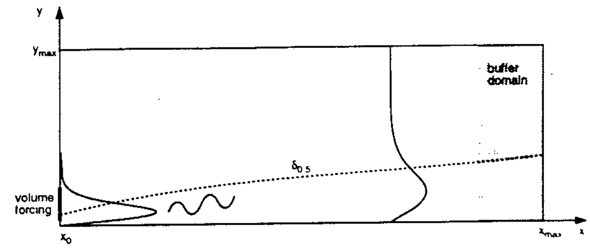

Figure 1: Computational domain with schematic of volume forcing for disturbance generation

2 Numerical Method

2.1 Governing equations

The governing equations are the two dimensional, incompressible, unsteady Navier–Stokes equations in vorticity-velocity formulation. The velocity components in the streamwise (x) and wall normal (y) directions are u and v, respectively (figure 1).

In these equations, the velocities are normalized by the jet exit velocity U_j, the spatial variables x, y by the nozzle width b, and the time by b/U_j. Taking the curl of the momentum equations, which eliminates the pressure gradient terms, yields the transport equations for the vorticity,

$$\frac{\partial\overline{\vec{\omega}}}{\partial t} + \nabla\times\left(\overline{\vec{\omega}}\times\overline{\vec{V}} - \nabla\cdot\vec{\vec{\tau}}\right) = \frac{1}{Re_J}\nabla^2\overline{\vec{\omega}}, \qquad (1)$$

where the overbar denotes an averaging operation (temporal or spatial). $\vec{\vec{\tau}} = [\tau_{ij}]$ is the turbulent stress tensor. In the two-dimensional case, this set of equations reduces to one equation for the spanwise vorticity component ω_z. The velocity components are computed from a set of Poisson equations (see [9] for more details).

In order to close equation (1), the turbulent stress tensor components τ_{ij} need to be modelled. The model used in this investigation is our new FSM. Following Speziale [5], the turbulent stress tensor components are written as

$$\tau_{ij} = f(\Delta/L_k)\tau_{ij}^R, \qquad (2)$$

where τ_{ij}^R is the Reynolds stress tensor and $f(\Delta/L_k)$ is the contribution function. In the contribution function, Δ is the effective computational grid size and $L_k = \left(\nu^3/\epsilon\right)^{1/4}$ is the Kolmogorov length scale. Note that the contribution function depends on the ratio Δ/L_k), i.e., the physical resolution of the computation compared to a length scale of turbulence in the flow. The Reynolds stress τ_{ij}^R in equation (2) is computed using the anisotropic Algebraic Stress Model (ASM) of Gatski and Speziale [10],

$$\begin{aligned}\tau_{ij}^R = & \frac{2}{3}K\delta_{ij} \\ & -f(\eta,\xi)\left[\alpha_1\frac{k^2}{\epsilon}\overline{S}_{ij}\right. \\ & +\alpha_2\frac{k^3}{\epsilon^2}\left(\overline{S}_{ik}\overline{W}_{kj}+\overline{S}_{jk}\overline{W}_{ki}\right) \\ & \left.-\alpha_3\frac{k^3}{\epsilon^2}\left(\overline{S}_{ik}\overline{S}_{kj}-\frac{1}{3}\overline{S}_{kl}\overline{S}_{kl}\delta_{ij}\right)\right]. \quad (3)\end{aligned}$$

The strain rate tensor and vorticity tensor are given by

$$\overline{S}_{ij}=\frac{1}{2}\left(\frac{\partial\overline{u}_i}{\partial x_j}+\frac{\partial\overline{u}_j}{\partial x_i}\right),\overline{W}_{ij}=\frac{1}{2}\left(\frac{\partial\overline{u}_i}{\partial x_j}-\frac{\partial\overline{u}_j}{\partial x_i}\right). \quad (4)$$

The function $f(\eta,\xi)$, in conjunction with k^2/ϵ, assumes the role of a nonlinear eddy viscosity,

$$f(\eta,\xi)=\frac{3}{3-2\eta^2+6\xi^2}\approx\frac{3(1+\eta^2)}{3+\eta^2+6\eta^2\xi^2+6\xi^2}, \quad (5)$$

where the expression on the right hand side of equation 5 is a regularized form of $f(\eta,\xi)$, which is used to avoid a possible division by zero in the original expression [5].

η and ξ are invariants of the irrotational strain rate tensor and the vorticity tensor, respectively,

$$\eta=\frac{1}{2}\frac{\alpha_3}{\alpha_1}\frac{k}{\epsilon}\left(\overline{S}_{ij}\overline{S}_{ij}\right)^{1/2},\xi=\frac{\alpha_2}{\alpha_1}\frac{k}{\epsilon}\left(\overline{W}_{ij}\overline{W}_{ij}\right)^{1/2}. \quad (6)$$

The values of model constants in equations (3) and (6) are $\alpha_1 = 0.227$, $\alpha_2 = 0.0423$, and $\alpha_3 = 0.0396$.

The turbulent kinetic energy k and the turbulent dissipation rate ϵ in equation (3) are computed from the standard transport equations [11],

$$\frac{Dk}{Dt}=-\tau_{ij}\frac{\partial\overline{u}_i}{\partial x_j}-\epsilon+\frac{\partial}{\partial x_j}\left[\left(\frac{\nu_T}{\sigma_k}+\frac{1}{Re}\right)\frac{\partial k}{\partial x_j}\right] \quad (7)$$

$$\begin{aligned}\frac{D\epsilon}{Dt} = & -C_{\epsilon1}\frac{\epsilon}{k}\tau_{ij}\frac{\partial\overline{u}_i}{\partial x_j}-C_{\epsilon2}f_{\epsilon2}\frac{\epsilon^2}{k} \\ & +\frac{\partial}{\partial x_j}\left[\left(\frac{\nu_T}{\sigma_\epsilon}+\frac{1}{Re}\right)\frac{\partial\epsilon}{\partial x_j}\right]. \quad (8)\end{aligned}$$

The eddy-viscosity ν_T and the wall damping function $f_{\epsilon2}$ are defined as

$$\nu_T=C_\mu k^2/\epsilon, \quad f_{\epsilon2}=1-e^{-y\,Re\sqrt{k}/10}. \quad (9)$$

Finally, the constants needed for the solution of equations (7) through (9) are,

$$\begin{aligned}C_\mu = 0.09, \quad C_{\epsilon1} &= 1.44, \quad C_{\epsilon2} = 1.83, \\ \sigma_k = 1, \quad \sigma_\epsilon &= 1.3, \quad A^+ = 25.\end{aligned}$$

2.2 Numerical scheme

A detailed description of the numerical schemes used for the solution of equation (1) and the Poisson equations for the velocities is given in [9]. For the time integration, a fourth-order accurate explicit Runge-Kutta method is used. The derivatives in the streamwise direction are approximated by fourth-order compact upwind and downwind biased differences at consecutive time steps and wall-normal derivatives are computed with fourth-order accurate compact differences. Lastly, a fast Fourier solver is implemented for the solution of the velocity Poisson equations.

In addition to the solution of the vorticity transport equation and the velocity Poisson equations, FSM requires the simultaneous integration of the k and ϵ equations. For these equations, a second order ADI method is used for the time integration and second-order accurate difference stencils are employed for the streamwise and wall normal derivatives. The fourth-order accurate difference method used in the discretization of the vorticity transport equation is employed for the spatial derivatives of the turbulent stress tensor components (see equation (1)).

2.3 Initial and Boundary conditions

The governing equations are solved in the computational domain shown in Figure 1. At the inflow boundary, Dirichlet conditions are imposed for the vorticity, the velocity components, the turbulent kinetic energy and the turbulent dissipation rate. For the computations presented here, the inflow conditions are obtained from a solution of the boundary layer equations for the turbulent wall jet. At the wall $y = 0$, the no-slip, no-penetration conditions are imposed on the velocity. The turbulent kinetic energy is set to zero, and a Neumann condition is used for the turbulent dissipation rate. At the free stream boundary $y = y_{max}$, a decay condition is imposed on v, and the wall normal derivative is set to zero for all other quantities. This requires the domain height to be large enough so that all disturbances have decayed sufficiently and the imposed boundary condition does not influence the solution.

Near the outflow boundary, a damping region similar to the one proposed by [12] is used. At the outflow boundary itself, all second derivatives are set to zero.

As initial condition, the vorticity, both velocity components, the turbulent kinetic energy and the turbulent dissipation rate are prescribed. These quantities are obtained from the solution of the boundary layer equations for the turbulent wall jet.

Disturbances are introduced into the flow using a volume forcing technique [13]. With this method, predominantly vortical disturbances can be generated anywhere in the flow field. In the cases presented in this paper, the volume force is applied near the inflow boundary and extends through most of the wall jet in the wall normal direction.

3 Results

3.1 Validation

Two-dimensional computations of the mean flow of the turbulent wall jet are used to validate our new FSM in the limit of traditional (steady) RANS. For the results shown here, the jet exit velocity is $U_j = 30\ \mathrm{m\,s^{-1}}$ and the nozzle height is $b = 5$ mm, which yields a jet exit Reynolds number $Re_j = 10000$.

The computational domain size is $40 < x < 240$, $y_{max} = 60$. 401 points are used in the streamwise x-direction, yielding $dx = 0.5$. With a timestep of $dt = 0.022$, the CFL number becomes $CFL = 0.044$. The wall normal direction is discretized using 200 points. Grid points are clustered near the wall which results in $dy = 0.00234$ at the wall. A grid refinement study with the boundary layer equation solver showed that this grid spacing gives grid independent results.

The computational results are compared with experimental data of Eriksson [14]. The experiments were conducted in a water tank. In the experiments, the jet exited at a velocity of $U_j = 1\ \mathrm{m\,s^{-1}}$ through a nozzle $b = 10$ mm high, which yields a jet exit Reynolds number of $Re_j = 10000$. For clarity, only the downstream location of $x/b = 140$ is shown in the following plots. These profiles are representative for a large section of the integration domain, excluding the regions close to the inflow and outflow boundaries.

The computed mean profile for the u-velocity is shown in figure 2 in outer coordinates. Overall, very good agreement with experimental data is achieved. The velocity maximum is located at $y/y_{1/2} = 0.13$, slightly closer to the wall than the experimental

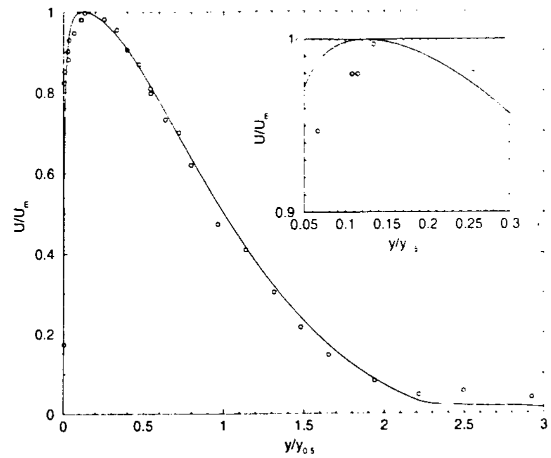

Figure 2: Streamwise velocity in outer coordinates. ∘ experimental results at $x/b = 70$ [14]

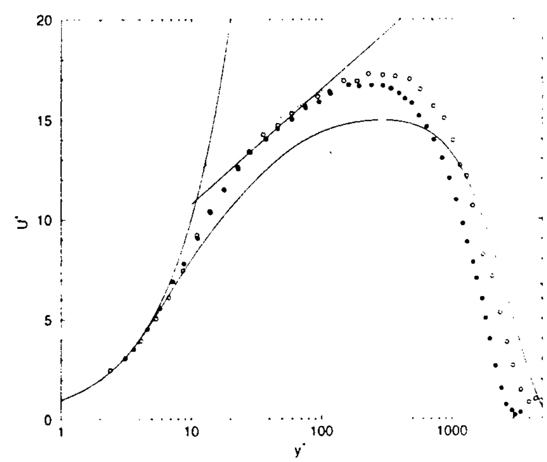

Figure 3: Streamwise velocity in wall coordinates. —— computational results, ∘ experimental results at $x/b = 70$, • at $x/b = 150$ [14]. ⋯ logarithmic law [17]

findings. When the u-velocity is plotted in inner coordinates ($u^+ = u/u_\tau$, $y^+ = yu_\tau/\nu$, $u_\tau = \sqrt{\tau_w/\rho}$, figure 3), it is seen that the viscous sublayer is resolved with about 5 points within $y^+ < 5$ and the results show excellent agreement with the theoretical curve $u^+ = y^+$. In the logarithmic layer, $u^+ = A \log y^+ + B$, the computed maximum u-velocity is slightly lower than the measured value and the theoretical prediction, a tendency which was observed for other $k - \epsilon$ models (see [15] and [16]).

Figure 4 shows the wall jet half width as a function of downstream distance. The downstream location is corrected for the location of the "virtual nozzle", which is determined such that the linear upstream extrapolation of $(U_j/U_m)^2$ is equal to one for $(x-x_0)/b=0$. In the case presented here, $x_0/b \approx 23$. The data are scaled using the normalization proposed in [18], where the length scale is ν^2/M and $M=U_j^2 b$ is the jet momentum at the nozzle exit. Excellent agreement with the experimental results is achieved. The spreading rate $dy_{1/2}/dx = 0.073$ matches the value given in [2].

The decay of the maximum jet velocity U_m is shown in figure 5, again normalized with the velocity scale $U = M/\nu$. The results are in very good agreement, although the computational results are slightly higher than the curve fit of the experimental data. A similar trend is observed in Schober [8] when his measurements are compared with the data by Wygnanski *et al.* [18].

In figure 6 the skin friction coefficient is plotted as a function of downstream distance. The computational results indicate a slightly lower decay rate than the curve fit in [18]. This yields skin friction values which are approximately 50% too high towards the downstream end of the computational domain. Schober [8] pointed out that his results are also in much better agreement with early results by Bradshaw & Gee [19], who found a higher skin friction than [18]. Unfortunately, the results in [19] cannot be converted to the scaling of figure 6. Therefore, figure 7 shows the local skin friction coefficient $c_f = \tau_w/(1/2\rho U_m^2)$ as a function of local maximum Reynolds number $Re_m = U_m y_m/\nu$. In these coordinates, the computational results are only about 20% higher than the curve fits reported in [19] and [20], and the streamwise development is in good agreement with their data. A similar deviation was reported for the $k-\epsilon$ model used in [21].

Results for the Reynolds shear stress R_{12} are shown in both inner and outer coordinates in figures 8 and 9. Excellent agreement between experiments and computations is achieved. Near the wall, $y/y_{1/2} < 0.4$, the experimental results are slightly underpredicted. This is observed more clearly in figure 9, where R_{12} is plotted in wall coordinates. Comparing the experimental results in figure 9 and figure 3 shows the well known nonequilibrium nature of the wall jet, indicated by the displacement of the location of zero Reynolds shear stress from the location of maximum velocity. An equilibrium turbulence model like the ASM model used in this investigation cannot predict this effect since $R_{12} \propto S_{12}$. This could explain the deviation of the computed R_{12} profiles from the experimental

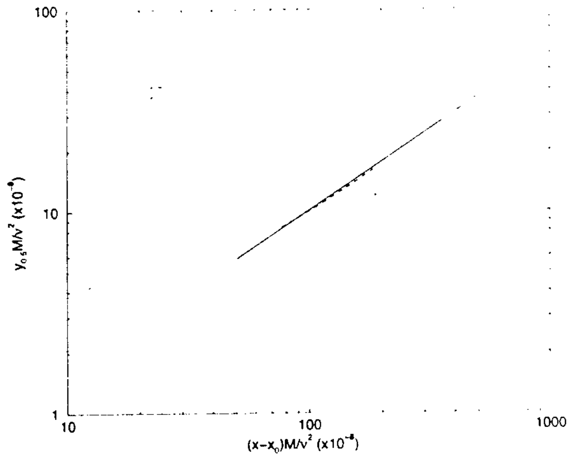

Figure 4: Normalized jet half width as a function of normalized downstream distance. —— curve fit by [18], ··· computational results

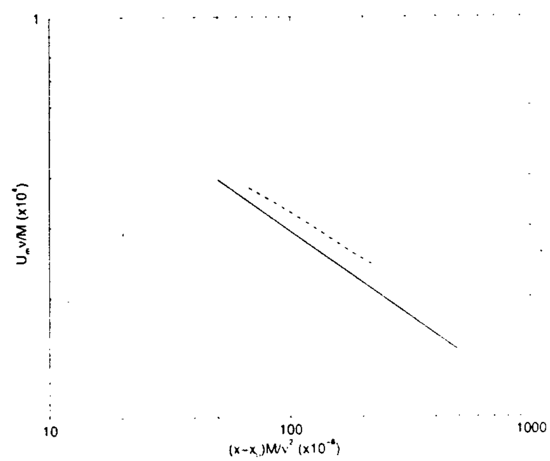

Figure 5: Normalized local maximum velocity as a function of normalized downstream distance. —— curve fit by [18], ··· computational results

results. In addition, this could also affect the location of the velocity maximum, which is slightly closer to the wall ($y_m/y_{1/2} = 0.13$) than the average of experimental findings, $y_m/y_{1/2} \approx 0.15$ (see inset in figure 2).

Figures 10 and 11 show the streamwise and wall normal Reynolds stress components. Comparing figures 10 and 11, it becomes clear that the turbulence model used in the computation is indeed able to predict the anisotropy in the turbulent wall jet.

To summarize, very good agreement was achieved between experimental findings and the computational results. However, some of the shortcomings

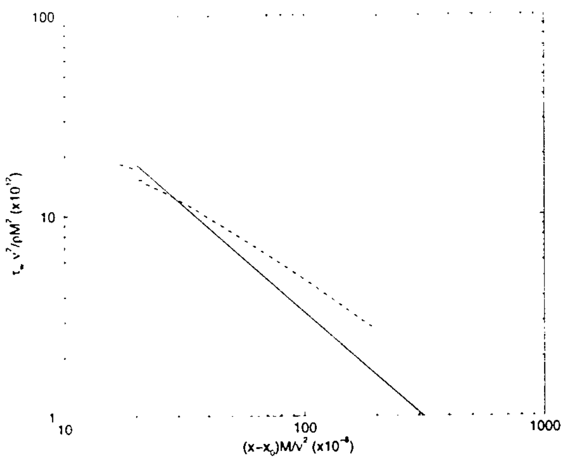

Figure 6: Normalized skin friction coefficient as a function of normalized downstream distance. —— curve fit by [18], ··· computational results

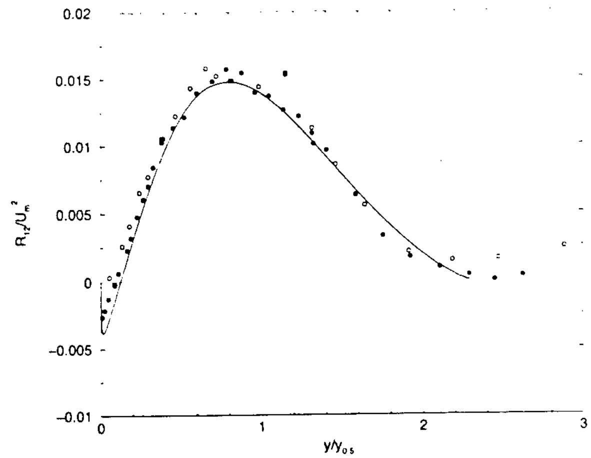

Figure 8: Reynolds shear stress, R_{12}, in outer coordinates. —— computational results, $\circ$ experimental results at $x/b = 70$, $\bullet$ at $x/b = 150$ [14]

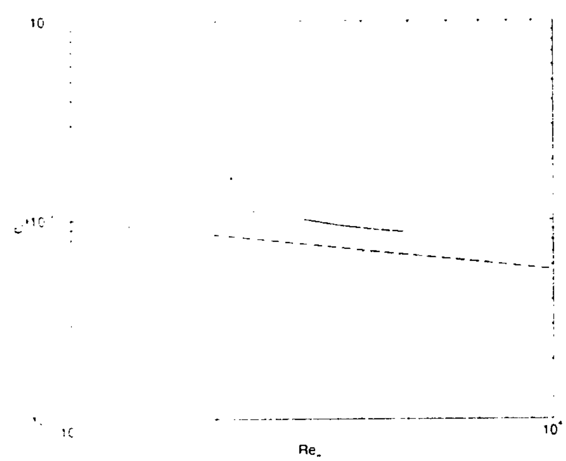

Figure 7: Local skin friction coefficient $c_f = \tau_w/(1/2\rho U_m^{2})$ as a function of local Reynolds number $Re_m = U_m y_m/\nu$. —— computational results, ··· curve fit by [19], - - - curve fit by [20]

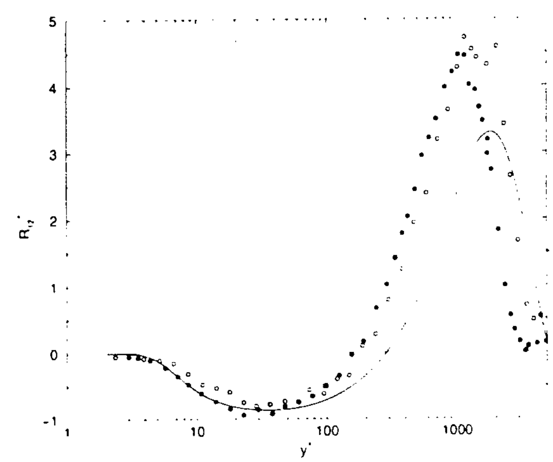

Figure 9: Reynolds shear stress, R_{12}, in wall coordinates. —— computational results, $\circ$ experimental results at $x/b = 70$, $\bullet$ at $x/b = 150$ [14]

of the turbulence model become apparent. First, although anisotropic effects are included in the model, the distribution of the streamwise Reynolds stress R_{11} shows considerable deviations in the near wall region. And second, the non-equilibrium nature of the turbulent wall jet cannot be captured with an ASM model of the form of equation (3) (or any other equilibrium $k - \epsilon$ model).

3.2 Effect of forcing on the turbulent wall jet

Using the Flow Simulation Methodology (FSM) in the unsteady RANS limit, the effect of large coherent structures on the turbulent wall jet was investigated. Even though FSM was developed to be used as a subgrid scale turbulence model, it is of particular importance that computations in the unsteady RANS limit yield accurate results. The disturbances are introduced into the turbulent base flow using the volume forcing method described in section 2.3.

In experiments with periodic forcing by Katz

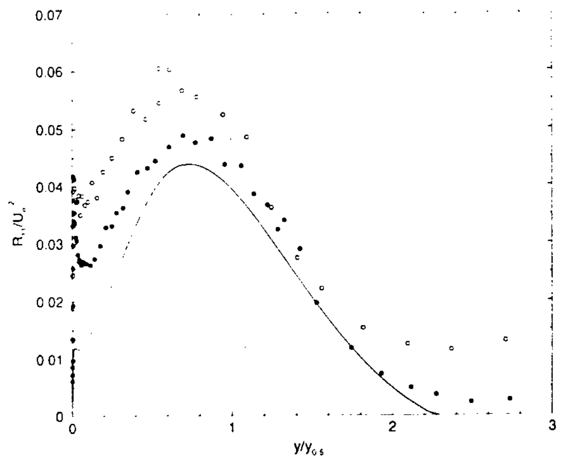

Figure 10: Streamwise component of the Reynolds stress, R_{11}, in outer coordinates. —— computational results. ∘ experimental results at $x/b = 70$, • at $x/b = 150$ [14]

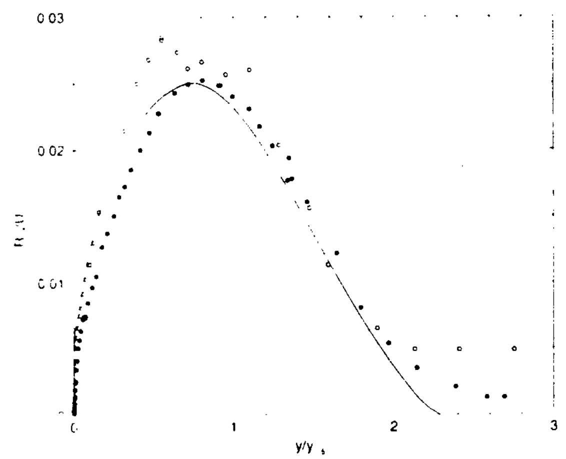

Figure 11: Normal component of the Reynolds stress, R_{22}, in outer coordinates. —— computational results. ∘ experimental results at $x/b = 70$, • at $x/b = 150$ [14]

et al. [6], a skin friction reduction on the order of 10% was achieved with a forcing amplitude of only 5%. From the large coherent structures observed in a flow visualization of the turbulent wall jet, they concluded that an instability of the turbulent wall jet exists. They also showed that the natural unforced turbulent wall jet has a strong spanwise coherence, which is increased considerably by periodic forcing. If these coherent structures are in fact nearly two-dimensional, a two-dimensional simulation should be sufficient to investigate the effect of periodic forcing on the large coherent structures,

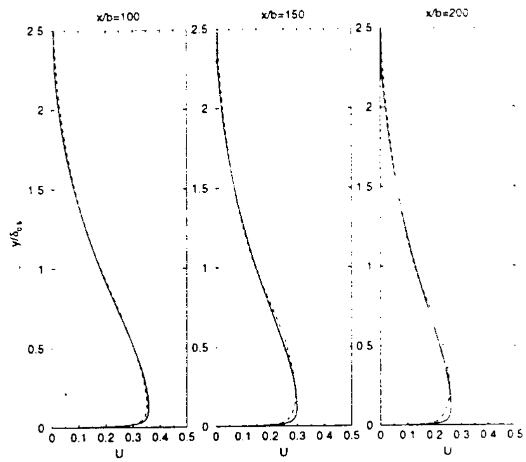

Figure 12: Effect of large scale structures on the mean u-velocity profile. —— Base Flow, ··· Case02, - - - Case03

Case	$\hat{f}/U_j$
Case01	5×10^{-3}
Case02	1×10^{-2}
Case03	2×10^{-2}

Table 1: Disturbance amplitudes. Forcing frequency $\beta_j = 0.0028$.

and as a consequency, on the mean flow of the turbulent wall jet.

The forcing frequency was chosen at $\beta_j = 0.0028$ ($f = 17Hz$). Table 1 shows the forcing amplitudes for the cases described in the following. Figure 12 compares the mean flow profiles of Case02 and Case03 with the profile of the undisturbed base flow at $x/b = 100, 150, 200$. In Case03, the large forcing amplitudes cause a significant mean flow distortion. Note that this mean flow distortion increases in streamwise direction, indicating that the disturbances in the flow actually enable an energy transfer from the mean flow to the large, coherent structures.

The reduction of the skin friction is shown in figure 13, where $c_f = \tau_w/(1/2\rho U_m^2)$ is plotted as a function of downstream distance x/b. As the forcing amplitude is increased, the deviation from the undisturbed base flow increases significantly, not only in magnitude but also in streamwise extent. For Case03, the skin friction reduction is comparable to the experimentally observed values.

To shed some light on how the large, coherent structures influence the mean flow, figure 14 shows

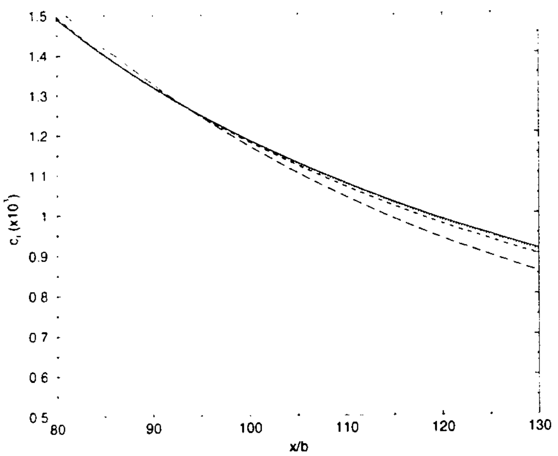

Figure 13: Skin friction c_f as a function of downstream distance. —— Base flow, ··· Case01, - - - Case02. -·-·- CaseB03

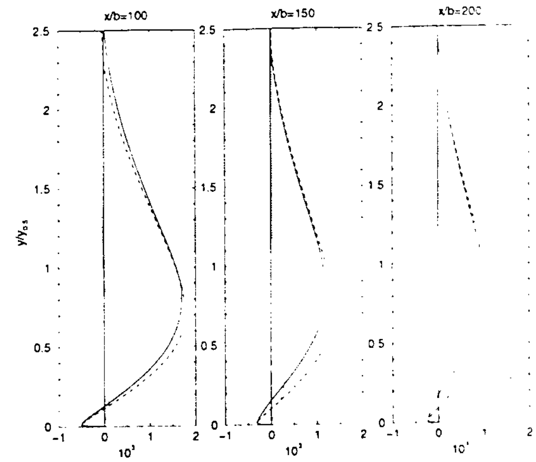

Figure 14: Reynolds stresss R_{12}. —— random part (modelled), ··· coherent part, - - - sum of coherent and random parts

the Reynolds shear stress contribution of the coherent motion, $\overline{u'v'}_c$, the Reynolds stress of the modelled small scales, R_{12}, and the sum $\overline{u'v'}_c + R_{12}$ for Case03. The figure clearly shows how the large scale structures increase the Reynolds stress from very close to the wall to about the wall jet half width and have very little effect in the outer part of the shear layer. As can be seen from the figure, this also means that the y location of the zero of the Reynolds stress is now displaced from the location of the velocity maximum towards the wall. The displacement is in surprisingly good agreement with experimental findings ($y_{R_{12}=0} \approx 0.6 y_{1/2}$ at $x/b = 200$). This shift has so far been attributed to nonequilibrium effects and its origin and importance has been the subject of considerable controversy. The simulations presented here indicate that the large unsteady shear layer structures, in conjunction with their nonlinearly created harmonics, are a major contributor to this effect. Figure 15 shows a comparison of R_{12} from the ASM model without large scale structures, the sum $\overline{u'v'}_c + R_{12}$, and experimental results of Eriksson *et al.* [14].

The local increase in the Reynolds shear stress leads to an increase in the spreading of the turbulent wall jet and a reduction of the maximum local jet velocity (see figure 12). Both these effects lead to the reduction of the slope of the velocity profile at the wall, reducing the skin friction.

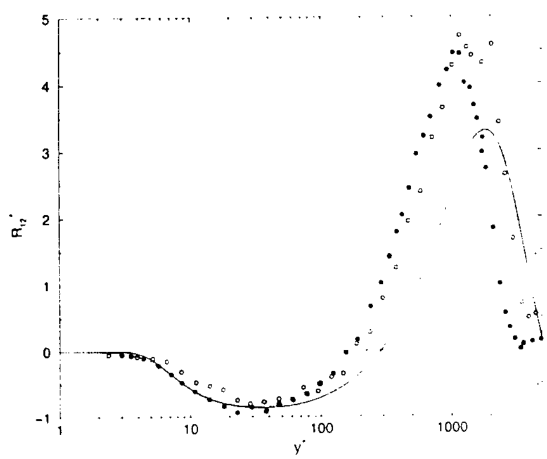

Figure 15: Reynolds stresss R_{12} in inner coordinates. —— Mean flow without large structures. ··· Mean flow with large structures. ∘ experimental results at $x/b = 70$, • at $x/b = 150$ [14]

4 Concluding Remarks

In this paper, the effect of large, coherent structures on the mean flow of the turbulent wall jet is investigated with our new Flow Simulation Methodology (FSM). For these investigations, FSM was used in the limit of unsteady RANS.

Excellent agreement between experimental and computational results was achieved. The results show that the large scale motion plays a key role in the transport of momentum in the wall normal direction. This is most clearly shown by the displacement of the location of zero Reynolds shear stress from the location of maximum velocity. It is interesting to note that the effect of the structures in the shear layer is felt very close to the wall, indicating a strong coupling between the boundary layer and the shear layer regions. The computational results presented in this paper suggest that these structures are not just being convected downstream passively, but instead continuously interact with the mean flow, extracting kinetic energy and redistributing momentum in the flow. In addition, the computations presented in this paper show that the Flow Simulation Methodology in the limit of unsteady RANS is indeed capable of accurately reproducing the large coherent motion in the turbulent wall jet.

Acknowledgement

This work was supported by the Air Force Office of Scientific Research, under grant number F49620-97-1-0274. T. Beutner served as the technical monitor.

References

[1] I. Wygnanski. Boundary layer and flow control by periodic addition of momentum (invited). *AIAA Paper*, 97-2117, 1997.

[2] B. E. Launder and W. Rodi. The turbulent wall jet. *Prog. Aerospace Sci.*, 19:81–128, 1981.

[3] B. E. Launder and W. Rodi. The turbulent wall jet — measurements and modeling. *Ann. Rev. Fluid Mech*, 15:429–459, 1983.

[4] M. E. Schneider and R. J. Goldstein. Laser doppler measurement of turbulence parameters in a two-dimensional plane wall jet. *Phys. Fluids*, 6(9):3116–3129, 1994.

[5] C. G. Speziale. Turbulence modeling for time-dependent RANS and VLES: A review. *AIAA J*, 26:173–184, 1998.

[6] Y. Katz, E. Horev, and I Wygnanski. The forced turbulent wall jet. *J. Fluid Mech.*, 242:577–609, 1992.

[7] M. D. Zhou, C. Heine, and I. Wygnanski. The effects of excitation on the coherent and random motion in a plane wall jet. *J. Fluid Mech.*, 310:1–37, 1996.

[8] M. Schober. *Beeinflussung inkompressibler turbulenter Wandstrahlen.* PhD thesis, Technische Universität Berlin, 1999.

[9] H. Meitz and H. F. Fasel. A compact-difference scheme for the navier-stokes equations in vorticity-velocity formulation. *J. Comp. Phys.*, 157:371–403, 2000.

[10] T. B. Gatski and C. G. Speziale. On explicit algebraic stress models for complex turbulent flows. *J. Fluid Mech.*, 254:59–78, 1993.

[11] W. P. Jones and B. E. Launder. The prediction of laminarization with a two-equation model of turbulence. *Int. J. Heat Mass Transfer*, 15:301–314, 1972.

[12] M. Kloker, U. Konzelmann, and H. Fasel. Outflow boundary conditions for spatial naver-stokes simulations of transitional boundary layers. *AIAA J*, 31 (4), 1993.

[13] H. Meitz. *Numerical investigation of suction in a transitional flat-plate boundary layer.* PhD thesis, The University of Arizona, 1996.

[14] J. G. Eriksson, R. I. Karlsson, and J. Persson. An experimental study of a two-dimensional plane turbulent wall jet. *Exp. Fluids*, 25:50–60, 1998.

[15] G. P. Hammond. complete velocity profile and "optimum" skin friction formulas for the plane wall-jet. *J. Fl. Eng.*, 104(59):59–66, 1982.

[16] G. Gerodimos and R. M. C. So. Near-wall modeling of plane turbulent wall jets. *Journal of Fluids Engineering*, 119:304–313, 1997.

[17] P. Y. Nizou and T. Tida. Transferts de chaleur et de quantité de mouvement dans les jets pariétaux plans turbulents. *Int. J. Heat Mass Transfer*, 38(7):1187–1200, 1995.

[18] I. Wygnanski, Y. Katz, and E. Horev. On the applicability of various scaling laws to the turbulent wall jet. *J. Fluid Mech.*, 234:669–690, 1992.

[19] P. Bradshaw and M. T. Gee. Turbulent wall jets with and without an external stream. *Aero Res. Council R & M 3252*, 1960.

[20] A. Sigalla. Experimental data on turbulent wall jets. *Aircraft Engineering*, pages 131–134, 1958.

[21] H. I. Andersson, A. O. Braseth, and B. Holmedal. computation of the inlet wall jet in a rectangular enclosure. *Comp. Fluid Dyn.*, 1:217–232, 1993.